Design, Realization and Applications of Dynamically Controllable Bragg Gratings

Vom Fachbereich Physik
der Technischen Universität Darmstadt

zur Erlangung des Grades
eines Doktors der Naturwissenschaften
(Dr. rer. nat.)

genehmigte Dissertation von
M.Sc. Poonam Arora
aus Rohtak Haryana, Indien

Referent: Prof. Dr. T. Tschudi
Korreferent: Prof. Dr. G. Birkl

Tag der Einreichung: 16.10.2007
Tag der Prüfung: 19.12.2007

Darmstadt, 2007
D 17

Dedicated to Lord Shri Krishna and His eternal consort Shrimati Radharani.

Contents

Chapter 1

Introduction

"It is difficult to point to another single device that has brought more important experimental information to every field of science than the diffraction grating. The physicist, the astronomer, the chemist, the biologist, the metallurgist, all use it as a routine tool of unsurpassed accuracy and precision, as a detector of atomic species to determine the characteristics of heavenly bodies and the presence of atmospheres in the planets, to study the structures of molecules and atoms, and to obtain a thousand and one items of information without which modern science would be greatly handicapped."

- J. Strong, J. Opt. Soc. Am. 50 (1148-1152), quoting G. R. Harrison

Light and its characteristics have always raised intrusiveness. Due to the incessant desire of mankind to control light and its propagation for useful applications, there has been a tremendous development in the field of optics. From just being known for lenses and mirrors in earlier times, optics has now infiltrated into virtually all fields of science and technology. However, the biggest impact of development in optical technologies in the recent few decades has been seen in modern information technology and telecommunications. Perhaps one of the most significant scientific developments in the 21st century is optical communication. The invention of laser and optical fiber in the last century made it possible to send and retrieve information optically. The enormous bandwidth of the optical fiber is being utilized with techniques like wavelength division multiplexing (WDM) and time division multiplexing (TDM). Due to the increasing number of users and applications of optical communications, the demand for speed and bandwidth enhancement is growing rapidly. In order to cater to these growing requirements, new optical technologies are being explored for further bandwidth enhancements and for increasing the functionality of future optical networks. Recent few years have seen the evolution of faster reconfigurable optical communication networks and for the growth of such networks, the design and development of dynamical, tunable and reconfigurable optical devices and components has become indispensable. This fact motivates the work presented in this thesis.

Undeniably, a grating is the most-widely used optical component for controlling light prop-

agation via diffraction. Due to the inherited property of spectrally selective diffraction (usually limited to one strong order), Bragg gratings are extensively used as spectral filters in DWDM (Dense Wavelength Division Multiplexing) networks. However, the evolution of Bragg grating based devices into dynamically tunable and reconfigurable devices is necessary to make them compatible with future optical communication networks like OCDMA (Optical Code Division Multiple Access). On this account, this research is dedicated to the design and realization of Bragg gratings with fast dynamical control and manipulation of their diffraction characteristics, especially to enhance the performance and functionality of Bragg grating based devices such as optical switches and filters.

The presented work lays emphasis on electrical control of diffraction from Bragg gratings in bulk and integrated lithium niobate for switching and filtering applications. Two types of Bragg gratings are addressed in this work: volume holographic (photorefractive) and photolithographic (surface-relief or corrugated). The thesis begins with a discussion on the optimization of the crystal orientation and experimental geometry in order to have efficient electrical control of holographic elements in bulk crystals. After the demonstration of fast switching of bulk holographic elements, the implementation of electrical control for integrated Bragg gratings in order to realize fast tunable integrated optical filter will be proposed. Subsequently, a novel technique combining the electro-optical control and phase-shift keying of integrated Bragg gratings will be proposed. The enormous potential of the proposed electro-optical phase-shift keying will then be demonstrated for the realization of a dynamically reconfigurable integrated optical filter.

1.1 Brief History of Developments

The invention of diffraction grating dates back to 1786, when an American astronomer David Rittenhouse strung hair between finely threaded screws [1]. However, it is Joseph von Fraunhofer who in 1821 invented the diffraction grating in the form we know today. A grating is defined as periodic modulation of conductivity or permittivity or both of a dielectric medium. Such a periodic modulation affects the propagation of light in such a way that the energy is scattered into various discrete directions [2]. The amount by which energy is scattered in a particular direction or order depends on the wavelength of the light and the period of the grating.

A Bragg grating is usually a grating which obeys Bragg's law of diffraction. The most important property of a Bragg grating is that the diffraction from this grating is usually limited to one strong diffraction order. Due to this property, they are widely used as wavelength selective filters. The grating was named after the Bragg father-son duo who established the Bragg's law while investigating diffraction of x-rays from the atomic lattice of a solid crystal [3]. Because the atoms are assembled in a regular periodic array, the scattered x-rays from the lattice can constructively interfere at certain angles. The concept of constructive interference and wave propagation in periodic structures arises in a vari-

ety of physical situations including periodic antenna arrays, crystal diffraction, and even the quantum mechanical interaction of electrons within a semiconductor crystal. Apart from the naturally existing Bragg gratings as stated above, they are fabricated in several materials using various techniques developed over time.

Since the invention of Bragg grating in a fiber by K.O. Hill in 1978 [4], Bragg gratings have become indispensable for telecommunication and sensor systems. Volume holographic Bragg gratings realized in photorefractive crystals are widely used for storage, switching and filtering applications as discussed in the present thesis. Photolithographically produced Bragg gratings are being used almost in all integrated optical circuits for various devices such as lasers, sensors and filters as discussed in this work. The functionality of Bragg gratings can be further enhanced by controlling various parameters in the Bragg condition. By doing so, diffraction from a Bragg grating can be controlled and used for applications like switching and tuning. Various controls on the Bragg condition with wavelength, angle, space, phase and even hybrids have already been tested and well-proven. For the Bragg gratings realized in an electro-optic material, an external electric field can be used to change the average refractive index of the material and hence to control the diffraction. The electrical control of diffraction for volume gratings for storage applications was first reported in year 1978-79 [5, 6]. In addition to high spectral selectivity, narrow bandwidth [7, 8], electrically controllable Bragg gratings exhibit fast tunability. In this thesis, the electrical control of diffraction from integrated Bragg gratings is proposed for the realization of fast tunable and reconfigurable optical filters.

1.2 Aim and Scope of the Thesis

General aim of this work is the realization and investigation of electrically controllable Bragg gratings. As discussed in the section above, Bragg gratings are ideal wavelength selective filters due to their property to diffract light into one strong diffraction order. The quintessence of my thesis is the realization of fast electrically tunable and reconfigurable integrated optical filters based on Bragg gratings. To reach this goal, different types of Bragg gratings were realized and the electrical control of diffraction was tested and optimized. This work mainly considers two types of Bragg gratings: volume holographic (photorefractive) and photolithographic (surface relief). In the first step, volume holographic Bragg gratings were realized in $LiNbO_3$ crystals and electrical control of diffraction was investigated. Electrically switchable holographic lenses and mirrors were successfully realized in bulk $LiNbO_3$ crystals, with a switching time of about 100 μs. Detailed theoretical calculations were performed to use the optimal orientation of the crystal. Also, the optimum polarization and geometry were used for recording in order to obtain better electric field selectivity. The switching time of holograms with electrical control was estimated and switching of focal length as well as direction was demonstrated. Both these applications are important for practical purposes like reading/writing of holographic disks, optical scanning etc. Besides simple realization, electrically controlled diffraction gives the advantage

of fast switching. However, due to the larger dimensions in bulk optics, the switching time, depending on the electrical capacity of the system, is relatively large. In integrated optical implementation, however, electrical switching times can be pushed down to the nanosecond range due to reduced dimensions.

After a successful realization of electrically controllable Bragg gratings in bulk optics, photorefractive Bragg gratings were realized in Ti:$LiNbO_3$ channel waveguides in order to demonstrate a fast tunable optical filter. Though, tunable filters based on different physical principles are already available, faster tunable optical filters with narrower bandwidth are desirable for the rapidly growing high-speed, high-capactity communication networks. Fiber based filters such as fiber Bragg gratings [9] (FBGs) and Fabry Perot [10] are the most commercialized. For high demanding dynamics, micromachined [11] and acousto-optic [12] filters offer a good solution in the microsecond tuning range. For the next-generation ultra-high speed requirements in the nanosecond range, faster mechanisms are needed such as the electro-optic effect. In our approach for the realization of fast tunable filters, the electro-optic effect was exploited to tune the central wavelength of the filter. In addition to the photorefractive gratings, the electrical control was effectively used for tuning the transfer function of a photolithographically produced Bragg grating in lithium niobate waveguides. Such a technique offers continuous tuning of the narrow bandwidth (approx. 170 pm) filter transfer function which is faster than most of the other existing techniques. Integrated optical implementation makes such tunable grating based filters very promising for a variety of applications ranging from spectroscopy to optical sensors, tunable lasers and especially for DWDM telecommunication systems.

Furthermore, the nonlinear properties of photorefractive gratings were investigated in detail. Photorefractive charge transport is highly nonlinear, especially in the cases of high modulation depths. During the investigation of nonlinearities, efficient diffraction was observed from higher spatial harmonics of photorefractive gratings in reflection geometry, for the first time to the best of my knowledge.

The most important and interesting topic of the work was the introduced concept of electro-optical phase-shift keying for dynamic manipulation and reconfiguration of the filter transfer function. This novel concept comprises, for the first time to the best of my knowledge, the use of external electric field to dynamically inscribe phase-shifts to more than two sections of the already fabricated integrated corrugated Bragg grating. Employing this technique, a fast ($< 1\ \mu$s) reconfiguration or synthesis of the transfer function into several desirable profiles was demonstrated.

Wavelength division multiplexing scheme used in existing communication networks requires one dedicated wavelength per user. With the continued bandwidth requirements and due to the exhaust of available frequencies in the transmission window of transporting fibers, advanced multiplexing scheme like OCDMA has been developed for further bandwidth enhancements. Such networks require tunable and reconfigurable devices. An optical filter with enhanced functionality and a precise control over the profile and bandwidth of its transfer function is required not only for reconfigurable networks but also for wavelength

locking and stabilization of tunable lasers. The presented reconfigurable optical filters were specially designed for telecommunication applications. The biggest advantage of the proposed technique is that one single homogeneous grating is used to exhibit dynamic and fast control of the transfer function. There are no mechanical movements required for reconfiguring the transfer function unlike fiber Bragg grating and dynamic volume grating based filters, making the technique additionally fast (few GHz) and effective. Moreover, it offers a great deal of flexibility and dynamical control at the operational level as the induced phase-shifts are controlled by an externally applied voltage to the electrodes leading to a real-time reconfiguration of complex transfer function profiles. Using this technique, a spatial distribution of the applied electric field was applied to the grating instead of applying a homogeneous field as it was done for tuning the transfer function in the former investigations. For this purpose, eight pairs of electrodes were deposited onto the substrate surface on both sides of the waveguide grating leading to eight grating sections which can be shifted in phase with respect to each other. By applying different combinations of electrical voltages to different electrodes, a different amount of phase-shift can be introduced to each grating section and by doing this, the spectral transfer function can be tailored (or reconfigured or synthesized) as discussed in chapter 6.

1.3 Structure of the Thesis

The thesis is basically comprised of four major parts: a brief introduction to the necessary theoretical background, the presentation of electrically switchable bulk holographic elements, realization and investigation of integrated photorefractive and corrugated gratings and the presentation of electro-optical phase-shift keying for the realization of an integrated optical filter with tunable and reconfigurable transfer function. Each chapter starts with a brief introduction and a summary of its content. Chapter 2 and 3 form the basic theoretical background while chapters 4-6 include the major theoretical and experimental results.

In chapter 2, the basic theoretical background for volume holographic gratings is presented. This chapter intends to introduce Kogelnik's coupled wave theory which is most widely used to study diffraction characteristics of volume holographic gratings. Throughout this work, Bragg gratings have been read-out in reflection and so the case of reflection gratings have been specially addressed. This chapter also includes a short introduction to the multiplexing techniques as one such technique using an external electric field was later used to multiplex volume holograms in bulk crystals.

Chapter 3 introduces the theoretical base of the photorefractive effect which is used to realize volume holographic (refractive-index) gratings in bulk as well as in integrated lithium niobate samples. The basic understanding of the underlying effect is necessary before proceeding to the realization. The band-transport model describing the process of grating formation is discussed. In addition, the effect of photovoltaic field on grating formation was discussed specifically for lithium niobate.

The electrical control of volume photorefractive gratings is discussed in chapter 4. This chapter begins with issue of optimizing the crystal orientation and the experimental geometry in order to efficiently use the electrical control. The recording geometry and the configuration of the electro-optical control has to be optimized in order to reduce the voltage requirements. The crystal orientation was optimized considering the the grating amplitude and the effective electro-optic coefficient. The experimental technique to multiplex holograms of lenses and mirrors is outlined in detail. The switching time analysis manifests the potential of the electrical control. The limitations of the used geometry and the technique discussed at the end of this chapter motivate the following chapter.

Chapter 5 begins with the advantages of the integrated optical implementation relative to the bulk one. A brief introduction to the waveguide theory and coupling techniques is included to provide the basic understanding of integrated optical structures. A short introduction to the theory of waveguide gratings is necessary for the design of the required grating profiles. The design and realization of photorefractive waveguide gratings is discussed in detail. The measured results have been compared to the theoretically predicted results. The limitations of photorefractive gratings are described which motivates the next section on photolithographically produced Bragg gratings. The design issues, the fabrication steps and the challenges faced during fabrication of corrugated waveguide gratings are presented in detail. The measurements with the realized grating filter demonstrating the tunable transfer function are presented. The idea of using an array of such gratings in order to realize a wavelength demultiplexer is demonstrated with the measurement done on two such filters attached in series. A comprehensive discussion on various parameters of the realized filter concerning the requirements of the DWDM networks is presented. This chapter concludes with detailed discussion on the results of the investigation of nonlinear properties of integrated photorefractive gratings.

The functionality of electrically tunable integrated Bragg gratings was extended using the electro-optical phase-shift keying technique introduced in chapter 6. This chapter comprises the most significant results concerning the dynamic manipulation of the transfer function profile. It is intended to introduce the reader with various aspects of the phase-shift keying technique. An extensive overview of the existing techniques is presented before proposing the used technique. Relative advantages expected from the proposed technique are demonstrated with the experimentally measured results. The predictions made using the numerical simulations are confirmed with the measured results and various interesting reconfigurations of the transfer function have been presented. The switching time analysis manifests the potential of the proposed technique in providing a real-time dynamical control over the transfer function profile. The chapter concludes on a positive note mentioning the potential applications based on the proposed phase-shift keying technique.

Chapter 7 contains the summary of the results of the investigated topics and also includes an outlook to provide a basis for further investigations and applications. The attached appendix is intended to provide additional information about the material properties of lithium niobate.

Chapter 2

Volume Holography

The material used in most early experiments in holography was photographic film, which is generally a thin, two-dimensional layer of recording material. The holograms recorded inside the photographic film were essentially planar and thus lacked the sensitivity to changes in the angle of the reconstructed beam. The development of 3-dimensional holography in 1962 by Denisyuk improved the quality of the reconstructed image by taking the advantage of Bragg effect to attenuate the unwanted conjugate component of the reconstructed image. The following chapter contains a brief introduction on the types of holograms and also on holographic multiplexing techniques. A brief discussion on Kogelnik's coupled wave theory [13] for volume gratings predicting diffraction efficiency and Bragg selectivity is also included. A detailed description on volume holography can be found in books: "Volume Holography and Volume Gratings" by Solymar and Cooke [14] and "Optical Holography" by Collier, Burckhardt and Lin [15].

2.1 Introduction

Holography dates from 1948, when the British/Hungarian scientist Dennis Gabor developed the theory of holography while working to improve the resolution of an electron microscope [16]. He coined the term hologram from the Greek words holos, meaning "whole," and gramma, meaning "message." He proposed an approach to record and retrieve a wavefront in a manner that preserved both the phase and amplitude information of the original wave. The invention of the laser by Maiman in early 1960's gave a huge boost to holography. The high spatial and temporal coherence of a laser provided the high interference contrast needed for holography. In 1962, Leith and Upatnieks realized that the holography could be used as a 3-D visual medium. They significantly improved upon Gabor's idea by using laser and angular offset between interfering beams to allow various diffracted components of output light to be spatially separated, resulting in the first laser transmission of a hologram of a 3-D object with good reconstruction quality [15]. Since then, holography has firmly

established its potential in information storage, interferometry [17], microscopy, security systems, data processing and even in telecommunications [7].

2.2 Hologram Types

A hologram in itself is a diffracting object for bending and focusing light in such a way to create a 3D view. It uses the interference of monochromatic object and reference waves to record and reproduce multiple images for a 3-D view. A hologram can be classified as behaving like a plane diffraction grating or a volume diffraction grating. A simple grating can be considered as the degenerate case of a hologram. On the other hand, simple 2D holograms is also termed as photographically produced grating [18]. However, due to the additional recording of the information of the phase of the reflected light, unlike photography, a hologram creates everything that eyes can see − depth, size, shape, texture, and relative position from many points of view. In general, term hologram can be replaced by grating.

There are numerous types of holograms and there are various ways of classifying them. Holograms can differ in the way in which they are produced and the way in which they store the information. For the particular case of silver halide type films, the holographic information is coded in the emulsion according to the localized microscopic differences in the absorption of light or by the amount of silver halide converted to silver atoms during exposure and development. This is referred to as an **absorption hologram**. The absorption pattern on the film corresponds to the amount of light incident on the plate during exposure. If that same hologram is put through a bleaching process it will then be termed a **phase hologram**. In a phase hologram, for the reconstruction of the information, the reference beam is phase modulated in order to reconstruct the wavefronts of the original objects. Photorefractive gratings are a good example of phase hologram. In absorption holograms the reference beam is diffracted by the small patterns of exposed emulsion in the form of silver residue. Phase holograms absorb less valuable reconstructing laser light than the absorption type and thus create a brighter image.

Furthermore, a hologram (or grating) can be differentiated as thick (or volume) and thin (or planar) hologram (or grating). A hologram is considered to be thick if the thickness of the recording medium is greater than the spacing between the interference fringes. Otherwise the hologram is considered a thin hologram. A dimensionless analytic factor helps to distinguish the two types; it is called Q-factor defined as:

$$Q = \frac{2\pi T\lambda}{n\Lambda^2} \tag{2.1}$$

where T is the thickness of the recording medium or length of the recorded grating, n is the refractive index of the recording medium, λ is the recording wavelength and Λ is the spacing between the interference fringes or grating period. If $Q \gg 1$, the hologram

is considered as **volume or thick** hologram and if $Q \ll 1$, it is considered as **planar or thin** hologram. This implies that for a given wavelength λ, a grating or hologram is termed as volume grating if its length T is much larger than the grating period Λ. The gratings used during this work in the majority of cases have a grating spacing of about 350 nm and length of about 8 mm. For the read-out wavelength of 1550 nm, the Q-factor for such gratings is approximately $2.8\text{X}10^5$ and therefore, all the gratings used during this work can be considered volume gratings.

Volume holograms are further categorized as transmission and reflection holograms. In **transmission** holograms, the grating planes are almost normal to the surface of the holographic medium. For the recording of such holograms, the object and the reference beam enter from the same side of the recording medium. These holograms form the image by transmitting a beam of light through the hologram. It is also known that the transmission holograms have a high angular selectivity. In **reflection** holograms, the grating planes are almost parallel to the surface of the holographic medium. For the recording of such holograms, the object and the reference beam enter from opposite sides of the recording medium. These holograms form an image by reflecting a beam from the grating planes in the recording medium. Such holograms are known to have a high spectral selectivity.

2.3 Diffraction from Volume Gratings

There are different diffraction models available for describing diffraction from volume and planar holograms. Diffraction from a planar hologram or grating leads to multiple diffraction orders and is determined by the Raman-Nath model [19]. On the other hand, diffraction from a volume hologram or grating leads to only one strong diffraction order and obeys the Bragg condition:

$$\Lambda = \frac{\lambda}{2n \sin \theta_B} \tag{2.2}$$

where θ_B is the Bragg angle (angle at which the incident light is 100% diffracted). As a consequence a volume hologram can only be reconstructed by reference beams with a certain angle of incidence and a certain wavelength. Also, because the interference pattern is recorded throughout the whole volume of the storage material, volume holograms are sensitive to changes in the propagation properties of the readout beam, which makes it possible to record multiple holograms (multiplexing) within the same volume of the material. Using the Bragg selectivity inherent to volume holography, multiple holograms can be stored and retrieved independently in the same volume by changing the propagation properties of the reference beam. As a result, the information storage capacity is increased by volume holography. Before proceeding to the applications of volume holography, it is interesting to analyze the diffraction behavior of volume holograms, which is best explained by Kogelnik's coupled-wave theory [13] as explained in the next section.

2.3.1 Coupled-wave Theory

The coupled wave theory takes its name from the form in which the solution is obtained for the wave equation. Unlike planar holograms, wave coupling (exchange of energy between the propagating waves) effects must be considered for volume holograms. Kogelnik developed the coupled-wave theory for volume holograms in 1969, predicting diffraction efficiency and Bragg selectivity for volume gratings, which gives best fit to experimental results [13, 15]. Kogelnik's theory is capable of not only predicting the selective response of the volume hologram but also carrying these predictions into the high diffraction efficiency regime. The theory predicts efficiencies which in certain cases approach 100 %, implying nearly total depletion of the illuminating wave. This approach has the merit of providing analytical as well as numerical results with high accuracy and is sufficiently flexible to describe the properties of a wide variety of volume holograms with and without absorption.

This theory consists of analyzing a set of coupled linear differential equations describing the amplitudes of the readout and the diffracted waves. It is basically concerned with the analysis of a hologram formed with two plane waves, i.e. a sinusoidal recording. Fig. 2.1 shows the geometry to be analyzed. Boundaries of the hologram are designated by the vertical traces in the x-direction, z=0 and z=T. For the analysis, one can consider the hologram to be formed so that planes which are loci of constant dielectric constant (considering only phase holograms) are oriented perpendicular to the xz plane. The value of the dielectric constant varies as a cosine function in the direction of the grating vector $\overrightarrow{\mathbf{K_g}}$ lying in the xz plane normal to the isophase planes separated by the periodic distance Λ. The grating vector $\overrightarrow{\mathbf{K_g}}$, normal to the planes, is considered to have the absolute value

$$K_g = \mid \overrightarrow{\mathbf{K_g}} \mid = 2\pi/\Lambda \tag{2.3}$$

To discuss the diffraction of a light beam from such a grating, let us consider a monochromatic plane readout wave of light with electric field vector polarized perpendicular to the plane of incidence, is incident on the hologram from the left. Once the wave is inside the hologram boundaries, its direction of propagation is represented by the vector $\overrightarrow{\rho}$. vector $\overrightarrow{\sigma}$ represents the direction of the diffracted wave.

Beginning the analysis of wave propagation in the thick hologram with Maxwell's equations for a non-magnetic material of permeability μ=1 and without optical loss, result in the wave (Helmholtz) equation

$$\nabla^2 \overrightarrow{\mathbf{E}} - \mu_0 \varepsilon_0 \varepsilon \frac{\partial^2 \overrightarrow{\mathbf{E}}}{\partial t^2} - \mu_0 \sigma \frac{\partial \overrightarrow{\mathbf{E}}}{\partial t} = 0 \tag{2.4}$$

It is assumed that the absorption is negligible and assume conductivity $\sigma = 0$. Further, the electric field vector $\overrightarrow{\mathbf{E}}$ for the plane waves polarized in x direction can be written as a scalar

$$E(y, z, t) = Re[a(y, z) exp(i\omega t)]. \tag{2.5}$$

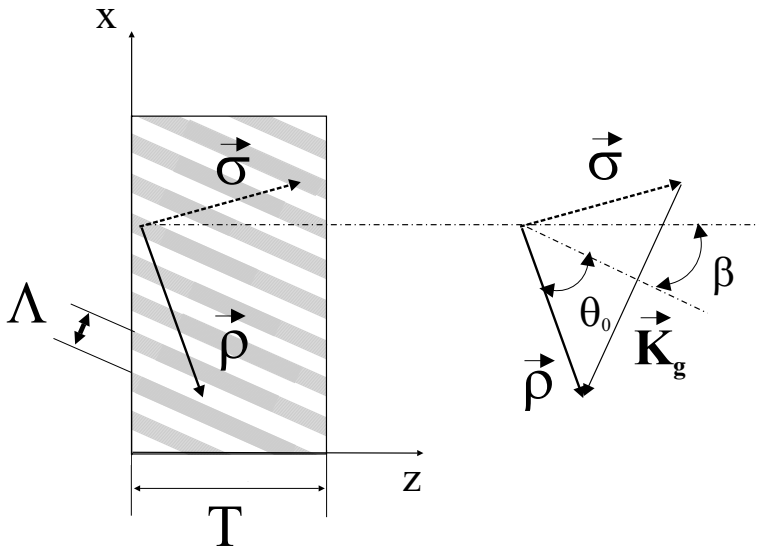

Figure 2.1: Geometry for the analysis of volume holograms.

Inserting eqn. (2.5) in eqn. (2.4), one obtains a partial differential equation for the complex wave amplitude

$$\nabla^2 a + q^2 a = 0 \tag{2.6}$$

where $q^2 = \frac{\omega^2}{c^2}\varepsilon(r)$ and where a is the complex amplitude of the light wave. ω is the frequency of the light wave, c is the speed of light, and ε is the dielectric permittivity of the medium.

A Bragg grating with sinusoidal refractive index modulation is considered. The spatial distribution of dielectric constant can be expressed as

$$\varepsilon(r) = \varepsilon + \varepsilon_1 \cos \overrightarrow{K_g} \cdot \overrightarrow{r} \tag{2.7}$$

where ε is the average component and ε_1 is the sinusoidally varying component of the dielectric permittivity. Using this notation for the spatial variation of the dielectric permittivity, the factor q^2 is expressed as

$$q^2 = \beta^2 + 2\chi\beta[\exp(i\overrightarrow{K_g} \cdot \overrightarrow{r}) + \exp(-i\overrightarrow{K_g} \cdot \overrightarrow{r})] \tag{2.8}$$

where

$$\beta = \frac{\omega}{c}\sqrt{\varepsilon} = \frac{2\pi}{\lambda}\sqrt{\varepsilon} \tag{2.9}$$

and

$$\chi = \frac{1}{2}(\frac{\omega}{c}\frac{\varepsilon_1}{2\sqrt{\varepsilon}}). \tag{2.10}$$

β is a constant of propagation and χ is the coupling parameter which is of central importance to this theory. The coupling parameter χ describes the interaction between the incident and the diffracted waves inside the medium. For χ=0, there is no interaction and hence no diffraction.

The eqn. (2.7) can be rewritten in terms of the average refractive index as

$$n^2(\overrightarrow{r}) = (n + n_1 \cos \overrightarrow{K_g} \cdot \overrightarrow{r})^2 = \varepsilon + \varepsilon_1 \cos \overrightarrow{K_g} \cdot \overrightarrow{r}. \tag{2.11}$$

Assuming $n_1 \ll n$, the square of the index can be expanded to obtain $n = (\varepsilon)^2$ and

$$n_1 = \frac{\varepsilon_1}{2n} = \frac{\varepsilon_1}{2\sqrt{\varepsilon}}. \tag{2.12}$$

Substituting eqn. (2.12) in eqn. (2.10) yields the coupling coefficient as

$$\chi = \frac{\pi n_1}{\lambda}. \tag{2.13}$$

Now, the partial differential eqn. (2.6) will be solved. For this, two assumptions are considered: first, it will be solved only for such angles of incidence which are close to those satisfying the Bragg's condition and second, it is assumed that only two waves propagate in the hologram: the incident wave and the diffracted wave, which closely satisfy the Bragg's condition. This last assumption puts a lower limit on the hologram thickness for which the theory is valid.

Within the volume grating, the complex amplitude of the electric field of light at any point can be presented as a sum of two plane waves: the readout wave R and the diffracted wave S.

$$a = R(z) \exp(-i\overrightarrow{\rho} \cdot \overrightarrow{r}) + S(z) \exp(-i\overrightarrow{\sigma} \cdot \overrightarrow{r}) \tag{2.14}$$

ρ and σ are already defined earlier. The phase factors $\exp(-i\overrightarrow{\rho} \cdot \overrightarrow{r})$ and $\exp(-i\overrightarrow{\sigma} \cdot \overrightarrow{r})$ define the propagation of waves inside the media without variations of dielectric permittivity and without absorption. The variations of phase and amplitude defined by spatial variations of dielectric permittivity are contained in the amplitude coefficients R and S.

When the beam is incident on the hologram at Bragg angle, the vector relation

$$\overrightarrow{\sigma} = \overrightarrow{\rho} - \overrightarrow{K_g} \tag{2.15}$$

between the incident and the diffracted wave propagation factors and the grating vector takes on a particular significance. In this case, $\overrightarrow{\rho}$, $\overrightarrow{\sigma}$ and $\overrightarrow{K_g}$ form an isosceles triangle of coplanar vectors. So $\rho = \sigma = \beta$ and

$$K_g/2 = \rho \sin \theta_0. \tag{2.16}$$

which can be written in the form

$$2\Lambda \sin\theta_0 = \lambda/n \quad (\mathbf{Bragg's Law}). \tag{2.17}$$

Eqn. (2.17) is then an expression of Bragg's law for light incident at the Bragg angle.

Returning to the problem of solving the wave equation, inserting eqn. (2.14) in eqn. (2.6), one obtains

$$R'' - 2i\rho_z R' - \rho^2 R + \beta^2 R + 2\chi\beta S = 0 \tag{2.18}$$

$$S'' - 2i\sigma_z S' - \sigma^2 S + \beta^2 S + 2\chi\beta R = 0. \tag{2.19}$$

The primes denote differentiation with respect to z and ρ_z and σ_z are projections along z direction. By making some reasonable assumptions and introducing useful notations, we can simplify eqns. (2.18) and (2.19). We now assume that $R(z)$ and $S(z)$ change slowly enough that R'' ($R'' \ll \rho_z R'$) and S'' ($S'' \ll \sigma_z S'$) can be neglected (slowly varying envelope approximation(SVEA)). Further, introducing some notations

$$C_R = \frac{\rho_z}{\beta}; \quad C_S = \frac{\sigma_z}{\beta}; \qquad \Gamma = \frac{\beta^2 - \sigma^2}{2\beta} \tag{2.20}$$

we can arrange eqns. (2.18) and (2.19) in the form

$$C_R R' = -i\chi S \tag{2.21}$$

$$C_S S' + i\Gamma S = -i\chi R \tag{2.22}$$

where $R' = dR/dz$ and $S' = dS/dz$.

The physics of the diffraction process is revealed by above coupled wave equations. For every increment of distance dz representing the progress of the incident and the diffracted waves through the thickness of the hologram, the wave complex amplitudes change by dR or dS. Changes are caused by coupling of one wave to the other by the terms χS and χR. But the term $i\Gamma S$ produces an additional phase factor in the diffracted wave. If the incident wave direction deviates too much from the Bragg angle, the factor Γ will be large. Then accumulation of this extra phase by the diffracted wave tends to force it out of synchronism with the incident wave and to cause the interaction to cease.

Eqns. (2.21) and (2.22) represent a system of two linear first-order differential equations. Substituting eqn. (2.21) into (2.22) produces one second-order differential equation for R

$$R'' + i\frac{\Gamma}{C_S}R' + \frac{\chi^2}{C_S C_R}R = 0 \tag{2.23}$$

A general solution of a second-order differential equation with constant coefficients has the form

$$R(z) = \exp(\gamma z). \tag{2.24}$$

Inserting eqn. (2.24) into eqn. (2.23) gives a quadratic equation for γ, which when solved yields the roots

$$\gamma_{1,2} = -\frac{i}{2}\frac{\Gamma}{C_S} \pm \frac{1}{2}\sqrt{\left(i\frac{\Gamma}{C_S}^2 - \frac{4\chi^2}{C_R C_S}\right)}. \tag{2.25}$$

Particular solutions to the eqn. (2.23) are $\exp(\gamma_1 z)$ and $\exp(\gamma_2 z)$, and a complete solution is the sum

$$R(z) = R_1 \exp(\gamma_1 z) + R_2 \exp(\gamma_2 z) \tag{2.26}$$

where R_1 and R_2 are constants which must be evaluated from the boundary conditions. Substituting eqn. (2.26) into eqn. (2.21), we obtain a similar equation for $S(z)$ as

$$S(z) = S_1 \exp(\gamma_1 z) + S_2 \exp(\gamma_2 z). \tag{2.27}$$

The constants R_1, R_2, S_1 and S_2 can be calculated for specific hologram geometries with appropriate boundary conditions. In the next section, these constants will be calculated for the case of reflection holograms which are mostly used for filtering applications and are addressed throughout this work.

2.3.2 Reflection Holograms

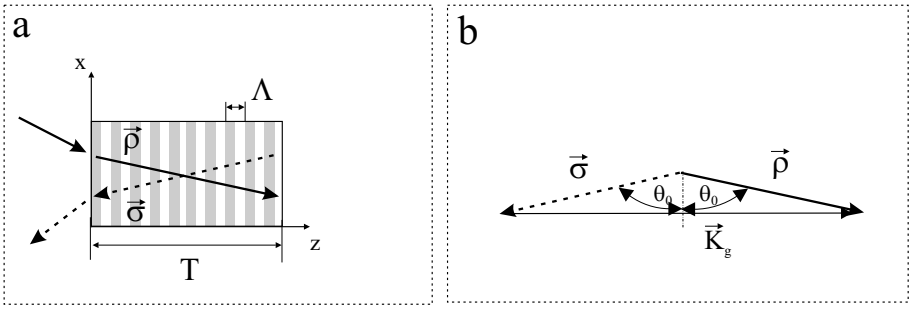

Figure 2.2: (a) Geometry of a reflection hologram with no slant, (b) Vector triangle relation at Bragg angle.

In this section, the coupled wave equations as derived in the previous section will be solved to calculate diffraction efficiency and wavelength selectivity for the particular case

of reflection holograms. When a reflection hologram is illuminated by a wave incident from the left, its response is characterized by a diffracted wave propagating from right to left. The amplitude of the diffracted wave is therefore zero at $z = T$. With the assumption of a unit amplitude for the incident wave, the boundary conditions take the form

$$R(0) = R_1 + R_2 = 1 \tag{2.28}$$

$$S(T) = S_1 \exp(\gamma_1 T) + S_2 \exp(\gamma_2 T) = 0. \tag{2.29}$$

These boundary conditions will be employed in the coupled wave equations in order to calculate the diffracted wave amplitude $S(0)$ emerging from the hologram at $z = 0$.

$$S(0) = S_1 + S_2 = -i\chi \left(i\Gamma + C_S \left[\frac{\gamma_1 \exp(\gamma_2 T) - \gamma_2 \exp(\gamma_1 T)}{\exp(\gamma_2 T) - \exp(\gamma_1 T)} \right] \right)^{-1}. \tag{2.30}$$

Now, eqn. (2.30) is evaluated under the conditions where the grating vector $\overrightarrow{K_g}$ is perpendicular to the surface of the grating as illustrated in Fig. 2.2, vectors $\overrightarrow{\rho}$, $\overrightarrow{\sigma}$ and $\overrightarrow{K_g}$ form an isosceles coplanar triangle at Bragg angle of incidence θ_0

$$C_R = \frac{\rho_z}{\beta} = -C_S = -\frac{\sigma_z}{\beta} = \sin\theta_0. \tag{2.31}$$

For simplification, some parameters are defined

$$\xi_r = \frac{\Gamma T}{2\sin\theta_0} = \frac{\beta T \delta \sin 2\theta_0}{2\sin\theta_0} = \delta\beta T \cos\theta_0 \tag{2.32}$$

$$\nu_r = \frac{\chi T}{\sin\theta_0} = \frac{\pi n_1 T}{\lambda \sin\theta_0}. \tag{2.33}$$

where δ is the detuning or mismatch parameter. To express $S(0)$ in terms of ξ_r and ν_r eqns. (2.31), (2.32) and (2.33) are substituted into the expression for $\gamma_{1,2}$ [eqn. (2.25)]

$$\gamma_{1,2} T = i\xi_r \pm \sqrt{(\nu_r^2 - \xi_r^2)}. \tag{2.34}$$

Substituting eqns. (2.32), (2.33) and (2.34) into eqn. (2.30) yields the amplitude of the diffracted wave at z=0,

$$S(0) = \frac{-i}{(i\xi_r/\nu_r) + \sqrt{1 - (\xi_r/\nu_r)^2}\coth(\sqrt{\nu_r^2 - \xi_r^2})} \tag{2.35}$$

and the diffraction efficiency is defined as

$$\eta = \frac{|\, S(0)\,|^2}{|\, R(0)\,|^2} = |\, S(0)\,|^2 = \frac{1}{(\xi_r/\nu_r)^2 + [1 - (\xi_r/\nu_r)^2]\coth^2(\sqrt{\nu_r^2 - \xi_r^2})}. \tag{2.36}$$

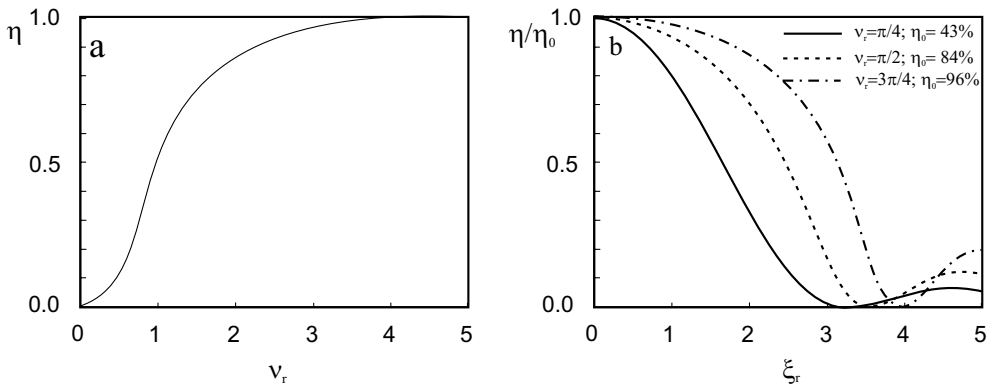

Figure 2.3: (a) Diffraction efficiency versus $\nu = \pi n_1 T/\lambda \sin\theta_0$ for the reflection phase hologram, (b) Relative efficiency η/η_0 of the lossless dielectric reflection hologram versus $\xi_r = \delta(2\pi n/\lambda)T\cos\theta_0$ for various values of the parameter $\nu = \pi n_1 T/\lambda\sin\theta_0$.

For Bragg incidence $\xi_r = 0$, and 100% diffraction efficiency is possible. The maximum possible efficiency is approached asymptotically with increasing ν_r as shown in Fig. 2.3 (a). Relative efficiency η/η_0 is plotted in Fig. 2.3 (b), as a function of ξ_r for three values of the parameter ν_r. For $\nu_r = \pi/4, \eta_0 = 43\%$; for $\nu_r = \pi/2, \eta_0 = 84\%$; and for $\nu_r = 3\pi/4, \eta_0 = 96\%$. Suppose we consider the $\nu_r = \pi/4$ curve and compute the wavelength selectivity of the reflection hologram. First, the detuning parameter δ is defined in terms of wavelength mismatch $\Delta\lambda$

$$\delta = -\frac{\Delta\lambda}{\lambda}\tan\theta_0 \tag{2.37}$$

Now, ξ_r takes the form

$$\xi_r = -\frac{\Delta\lambda}{\lambda}\beta T\sin\theta_0. \tag{2.38}$$

According to the curve corresponding to $\nu_r = \pi/4$ in Fig. 2.3 (b), $\eta/\eta_0 = 0$ when $\xi_r = 3.14$. For $\theta_0 = 90°$,

$$\frac{\Delta\lambda}{\lambda} = \frac{\Lambda}{T}. \tag{2.39}$$

To have a feeling for the numbers, suppose $\lambda = 532nm, T = 5mm, n = 2, \theta_0 = 30°$(in air), then solving for $\Delta\lambda$ in eqn. (2.38) yields $\mid \Delta\lambda \mid = 0.04pm$. This high degree of wavelength selectivity makes reflection holograms very attractive for filter applications.

2.4 Multiplexing Techniques

It is important to include a brief introduction to multiplexing techniques as they are very closely related to volume holograms especially for storage applications. During this work, however, only one such technique was used for switching and scanning application as discussed in chapter 4.

For volume holograms, the reconstructed beam or readout is highly sensitive to changes of the propagation properties in the readout beam. If the reference beam is modified sufficiently, the diffracted light contributions from different portion of the grating volume will lead to destructive interference effect and the diffraction from previously recorded holograms will be attenuated to zero. Then a new hologram can be written in the same volume of the recording medium with the new reference beam. So, one can exploit the angular selectivity and/or the wavelength selectivity as computed for reflection volume holograms in section 2.3.1 to multiplex holograms in a volume. Multiplexing techniques directly exploiting the Bragg condition for diffraction from volume holograms include angular multiplexing, wavelength multiplexing and electric field multiplexing. In addition, some more forms of multiplexing such as phase-shift multiplexing, shift multiplexing and hybrids of these techniques are also in use. All these multiplexing techniques have their respective advantages and limitations. Also, each of these give best results in a particular geometry of recording. For example, angular multiplexing is best when used with transmission holograms due to the advantage of high angular selectivity of such holograms. Wavelength multiplexing is best when used with reflection holograms due to the advantage of high wavelength selectivity of such holograms. More specific details of recording geometries are obtained for particular cases.

One of the aims of using multiplexing techniques, is to increase the storage capacity. Angular multiplexing has already proved its worth, when used for recording 5,000 holograms in a single lithium niobate crystal [20]. Wavelength multiplexing has also shown good results for storage [21] but the problem of finding tunable, highly coherent lasers with fast switching and large tuning range restricts its use for storage applications. Wavelength multiplexing is more popular for optical filter designs [22]. Phase-coded multiplexing [23] gives the same storage capacity as angular multiplexing but it has advantages of short readout times, high S/N ratio, high efficiency and possibility of performance of arithmetic operations. Due to this, phase-coded optical memories, high-capacity data storage and high-speed data processing becomes possible simultaneously.

Electric field multiplexing (EFM) [22, 24–26] allows to use one more degree of freedom. It involves changing the average refractive index of a holographic material by applying an external electric field. Since we are using photorefractive crystals which are inherently electro-optic materials, application of an external field to these crystals results in a change in refractive index, and hence in the Bragg condition. Most important advantages of this technique are fast switching, no mechanical movements involved and simple realization as one needs merely to apply different electric fields to record and reconstruct different holo-

grams. The change in refractive index of a material can be considered as equivalent change in wavelength inside the material. So, electrically controlled volume holograms can act as spectral filters. Due to this equivalence with spectral selectivity, reflection geometry is also best for EFM. The technique of EFM provides a spectral selectivity of recorded holographic filters up to a few picometers [26]. High efficiency of EFM was also demonstrated by electrically controlling, recording and retrieval of 17 holograms in lithium niobate [24]. Electrical multiplexing of 60 holograms in SBN [27] was also demonstrated but with much lower diffraction efficiency. Though EFM does not hold great promise for massive storage, its reproducibility and speed makes it preferable to use in other practical applications. During this work, this technique has been used for fast switching of holographic lenses and for fast directional switching (scanner application) and will be discussed in detail in chapter 4 .

Chapter 3

The Photorefractive Effect

The photorefractive effect is one of the most suitable effect for different volume holographic applications. This effect was used to form the majority of the used volume Bragg gratings. Several theoretical models describing the grating formation mechanism with this effect have been proposed. This chapter describes the photorefractive effect with the widely accepted band transport model by Kukhtarev [28] and presents the basic formulation and build up of the space-charge field. Detailed descriptions of the photorefractive phenomenon, materials and applications can be found in a number of books [29–33]

3.1 Introduction

Light-induced changes in optical properties such as refractive index and absorption coefficient are always related to material excitation, i.e. deviation from (thermal) equilibrium. Examples of material excitation are an increase in the number of conducting free electrons, the photon density or the number of electrons occupying excited states. As a result of spatially inhomogeneous material excitation, the optical properties become spatially modulated in the interference region of two intense coherent light waves and create gratings that may be permanent or dynamic, depending on the mechanism and the material [34].

While any grating can be ultimately reported to be a spatial modulation of the material's refractive index and/or absorption constant, one could cite various mechanisms for which light-matter interaction can produce optical gratings: for example, in semiconductors this creates a spatial modulation of the conduction electron density; in fluids the spatial modulation comes from molecular orientation; in mixtures it comes from the concentration; and in photorefractive materials it comes from the space charges and their associated fields [34].

3.1.1 Brief History of Developments

The photorefractive effect is a phenomenon in which the local index of refraction is changed by spatial variations of light intensity. Precisely, this effect is a combination of photoexcitation, formation of space-charge field by various transport processes and modulation of the refractive index via the linear electro-optic (Pockels effect) effect. It was first encountered in 1966 when A. Ashkin with his co-workers in Bell Labs were studying the transmission of laser beam through electro-optic $LiNbO_3$ crystal [35]. The wavefront of the transmitted beam was distorted by the refractive index variations caused by the propagating laser beam itself. They referred to it as "optical damage". However, about two years later, the potential of this new effect for use in high-density optical storage of data was realized by F. S. Chen and co-workers [36]. Since then, lot of attention has been devoted to photorefractive materials in order to understand the underlying mechanisms and to optimize these materials. Until 1990, the Photorefractive effect was observed in many inorganic electro-optic crystals such as $LiTaO_3$ (BSO), $BaTiO_3$, $KNbO_3$, SBN, in sillenite crystals such as $Bi_{12}SiO_{20}$, BGO, BTO and in some semiconductors such as GaAs, InP and CdTe. In 1990, this effect was first observed in organic materials namely single crystals of 2-cyclooctylamino-5-nitropyridine (COANP) doped with 7,7,8,8-tetracyanoquinodimetahne (TCNQ) [37]. This was followed by discovery of low cost photorefractive polymers in 1991 [38]. A great deal of efforts have been devoted to optimize these materials for various applications namely information storage [31,39], real-time holographic interferometry [40], optical phase conjugators [32], optical information processing [41] and narrow-band optical filters as presented in this work.

3.2 Photorefractive Nonlinear Optics

In the regime of linear optics, the index of refraction is independent of the intensity of light beam. When the light intensity becomes comparable to or more than the intra-atomic electric field, the distribution of electrons in the medium can be modified by the electric field of light and leads to a different index of refraction. This is the regime of nonlinear optics. In this regime, the propagation of light in the material can be controlled or manipulated by illumination of a light beam and this leads to variety of useful phenomenon such as optical parametric amplification, higher harmonic generation, stimulated Raman or Brillouin scattering etc. The photorefractive effect is also a nonlinear effect based on control of light by light. Here the index of refraction is changed by the spatial variation of the light intensity. Some of the electrons get excited and start to migrate through the material following the gradient of the non-homogeneous light intensity distribution and result in the creation of a space-charge distribution under non-homogeneous illumination. The linear electro-optic (Pockels) effect then translates the internal electric fields induced by the inhomogeneous space charges into a modulation of the material's refractive index.

According to the electromagnetic theory, the response (polarization) of a material to the

illumination (electric field) of light is described as

$$\mathbf{P} = \epsilon_0 \chi^{(1)} \mathbf{E} + \epsilon_0 \chi^{(2)} \mathbf{EE} + \epsilon_0 \chi^{(3)} \mathbf{EEE} + ... \tag{3.1}$$

where $\mathbf{P}$ is the induced polarization of the medium, ϵ_0 is the dielectric constant of vacuum, $\mathbf{E}$ is the electric field of the light and $\chi^{(i)}$ are the respective optical susceptibility tensors of rank $(i+1)$. $\chi^{(i>1)}$ tensors describe the nonlinear dependence of the polarization of the material on the incident light field. For the case of photorefractive materials, the second order susceptibility $\chi^{(2)}$ is considered which is responsible for the linear electro-optic or Pockels effect. Further details on nonlinear optical phenomenon can be found in [42].

3.3 Theoretical Models

Several models have been proposed to explain the grating formation mechanism in the photorefractive effect. A band transport model by Kukhtarev et. al. [28] in 1976 and a hopping model by Feinberg et. al. [43] in 1980 have been proposed for carrier movement. Fig. 3.1 shows the band transport model and the hopping model.

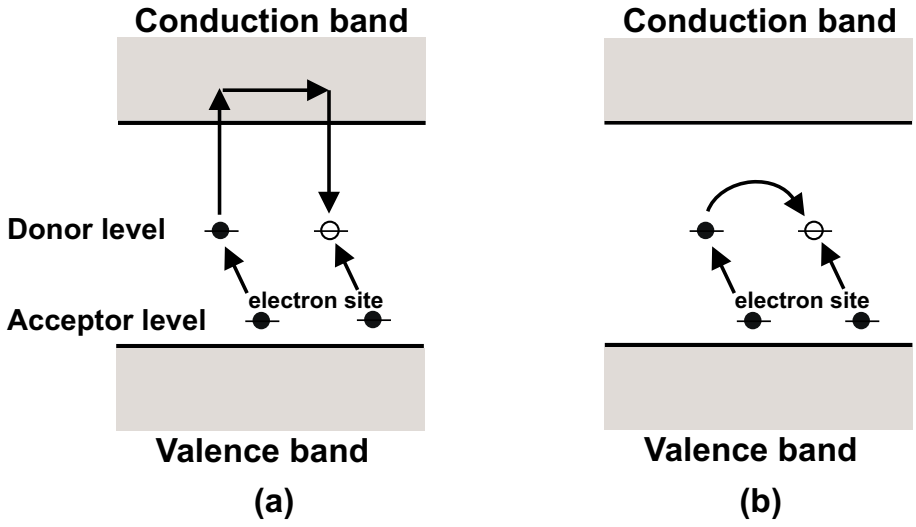

Figure 3.1: (a) The Band Transport Model, (b) The Hopping Model.

The band transport model is more versatile and explains almost all the observed photorefractive phenomenon. This model is discussed in little detail in the next section.

3.3.1 The Band Transport Model

For the sake of simplicity, it is assumed that all the donor impurities are identical and

have exactly the same energy state somewhere in the middle of the band gap. These donor impurities can be ionized by absorbing photons. As a result of ionization, electrons are generated in the conduction band leaving empty states behind. These ionized impurities are capable of capturing electrons.

It is assumed that the density of donor impurity be N_D, of which N_D^i are ionized. The rate of electron generation is $(sI+\beta)(N_D-N_D^i)$, whereas the rate of trap capture is $\gamma_R N N_D^i$, where N is the electron density, I is light intensity, β is rate of thermal generation of electrons, s is the cross section of photoexcitation, γ_R is the electron-ionized trap recombination rate. The rate equation for N_D^i is

$$\frac{\partial N_D^i}{\partial t} = (sI+\beta)(N_D - N_D^i) - \gamma_R N N_D^i. \tag{3.2}$$

For every impurity ionized there is an electron generated, an electron is eliminated when a recapture occurs which fills an empty impurity. The rate of generation of electrons is the same as that of the ionized impurities except that the electrons are mobile whereas the impurities are stationary. This is essential for the photorefractive effect. Supposing the light incidence at the input face (along x axis), the rate equation for electron density,

$$\frac{\partial N}{\partial t} - \frac{\partial N_D^i}{\partial t} = \frac{1}{q}\frac{\partial j}{\partial x} \tag{3.3}$$

where j is the current density and $-q$ is the electron charge. The presence of these charge carriers (electrons) leads to a space-charge field which in turn affects the transport of the carriers. The current density consists of contributions from drift of charge carriers due to an electric field, diffusion due to the gradient of carrier density and the photovoltaic current density and thus can be written

$$j(x) = qN(x)\mu E(x) + k_B T \mu \partial N(x)/\partial x + \alpha G I(x) \tag{3.4}$$

where μ is the mobility tensor, E is the electric field, $k_B T$ is the product of the Boltzmann constant and temperature. α is the absorption coefficient and G is the Glass constant characterizing the photovoltaic effect [33]. If the crystal is uniformly illuminated and open circuited, there will be a constant electric field in the crystal at steady state. The drift current due to this field will cancel the photovoltaic current. This constant field is called photovoltaic field

$$E_{ph} = -\frac{\alpha G N_A}{q\mu s(N_D - N_A)}. \tag{3.5}$$

The total electric field obeys the following Poisson equation:

$$\epsilon\frac{\partial E}{\partial x} = \frac{1}{\epsilon\epsilon_0}\rho(x) = -q(N + N_A - N_D^i) \tag{3.6}$$

ϵ is the dielectric constant, $\rho(x)$ is the charge density and N_A is the density of acceptor impurities. In the absence of illumination, the charge neutrality is written

$$(N + N_A - N_D^i) = 0 \tag{3.7}$$

In the case when the electron density is small, the density of ionized donor impurities equals the density of acceptor impurities. In eqn. (3.4), $qN(x)\mu E(x)$ represents the current density due to drift, $k_B T\mu\nabla N(x)$ is the current density due to diffusion and $\alpha GI(x)$ is the photovoltaic current density. The density of donors is most often larger than that of acceptor impurities. When there is no electron in the conduction band and no holes in valance band, the density of ionized donor impurities is identical to that of acceptor impurities. The neutral donor impurities are capable of donating electrons and ionized ones are capable of capturing these electrons. In this model the acceptor impurities are for the purpose of charge neutrality only. They do not directly participate in the photorefractive effect.

We now consider the incidence of two laser beams into a photorefractive medium. Let the electric field be written

$$E = E_a exp(i\omega t - i\overrightarrow{k}_a \cdot \overrightarrow{r}) + E_b exp(i\omega t - i\overrightarrow{k}_b \cdot \overrightarrow{r}) \tag{3.8}$$

where we assume that the frequencies of the beams are identical, E_a and E_b are amplitudes and $\overrightarrow{k}_a$ and $\overrightarrow{k}_b$ are wave vectors. If the polarization states are not orthogonal, they will form an interference pattern with an intensity given by

$$I(\overrightarrow{r}) = I_0 + Re\{I_1 e^{-i\overrightarrow{k}\cdot\overrightarrow{r}}\} \tag{3.9}$$

where

$$I_0 = \mid E_a \mid^2 + \mid E_b \mid^2 \tag{3.10}$$

$$I_1 = 2E_b \cdot E_a^* \tag{3.11}$$

where $\overrightarrow{K}$ is the grating vector defined as

$$\overrightarrow{K} = \overrightarrow{k_b} - \overrightarrow{k_a}. \tag{3.12}$$

The magnitude of the grating vector is related to the period (Λ) of the interference pattern by

$$K = \frac{2\pi}{\Lambda}. \tag{3.13}$$

If I_0 is the average light intensity which is constant both across the sample and in the input plane (along x axis), the light-intensity distribution recorded can be written as

$$I(\overrightarrow{r}) = I(x) = I_0[1 + m\cos(Kx)]. \tag{3.14}$$

In the bright regions, photo ionized charges are generated by absorption of photons. These charge carriers can diffuse away from bright regions leaving behind positively charged ionized donor impurities. If these charge carriers are trapped in the dark regions they will remain there because there is no light to re-excite them. This leads to charge separation. The dark regions become negatively charged and bright regions positively charged. The build up of space charge separation continues until the diffusion current is counter balanced by a drift current. The fundamental component of space charge density can thus be written as

$$\rho = \rho_0 \cos(Kx). \tag{3.15}$$

An integration of the Poisson eqn. (3.6) leads to

$$E = \rho_0 K \sin(Kx) \tag{3.16}$$

The space charge field is shifted in space by $\pi/2$ relative to the intensity pattern. This space charge field will induce a change in the index of refraction via the Pockels effect. Fig. 3.2 illustrates the spatial variation of the light intensity, space-charge density, space-charge field and the induced index change.

The photorefractive effect basically consists of three fundamental processes which occur in electro-optic crystals:

1. Photoionization of impurities leading to a generation of charge carriers and transport of these charge carriers.

2. Trapping of these charge carriers and formation of a space-charge density.

3. Photoinduced space-charge electric field leads to creation of an index grating via the Pockels effect.

3.4 Space Charge Field

To simplify the analysis, a low contrast ($m \ll 1$) of the recorded pattern is assumed. Again using the complex-function formalism for the light intensity

$$I(x) = I_0[1 + \frac{m}{2}\exp(iKx) + \frac{m}{2}\exp(-iKx)] \tag{3.17}$$

and the electric field $E(x)$,

$$E(x) = E_0 + E_{sc}(x) = E_0 + \frac{E_{sc}}{2}\exp(iKx) + \frac{E_{sc}^*}{2}\exp(-iKx)]. \tag{3.18}$$

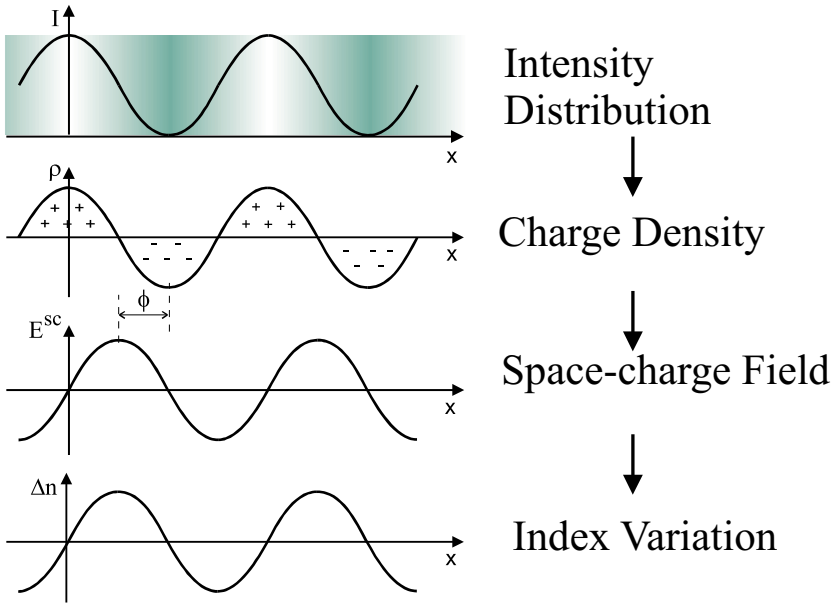

Figure 3.2: Formation of the refractive index grating from the spatial distribution of the light intensity

The basic equation giving the time evolution of the complex amplitude of the electric field grating E_{sc} can be obtained through a self-consistent solution of a set of equations. It includes, in particular, as first the poisson's equation:

$$\frac{\partial}{\partial x}E_{sc}(x) = \frac{1}{\epsilon\epsilon_0}\rho(x). \tag{3.19}$$

The second equation is the continuity equation describing the change of the charge density $\rho(x)$ at a given point

$$\frac{\partial}{\partial x}\rho(x) = -\frac{\partial}{\partial x}j(x). \tag{3.20}$$

The third equation is the balance equation for the electron density, as given by eqn. (3.3). From eqns. (3.3), (3.4), (3.19) and (3.20), we derive the fundamental equation that describes the formation of holograms, namely the time evolution of the electric field amplitude E_{sc}. eqns. (3.3) and (3.4) yield the following relation for the electron modulation depth in the conduction band

$$a = \frac{m(1 + iK\mu\tau E_{ph} + iK\mu\tau E_{sc})}{1 + K^2 D\tau - iK\mu\tau E_0} \tag{3.21}$$

where $E_{ph} = \alpha G/\sigma_0$ is the photovoltaic field established within the crystal by compensation of two opposite currents, namely the photovoltaic current ($= \alpha G I_0$) and the photoconductivity current ($= E_{ph}\sigma_0$ with $\sigma_0 = qN\mu$ being an average photoconductivity of the crystal).

Using eqns. (3.4), (3.19), (3.20) and (3.21), we get

$$\frac{\partial}{\partial t}E_{sc} = -\frac{m(iE_D + E_0 + E_{ph})}{\tau_M(1 + K^2L_D^2 - iKL_0)} \tag{3.22}$$

where $\tau_M = \epsilon\epsilon_0/\sigma_0$ is the characteristic Maxwell dielectric relaxation time of the crystal corresponding to its average photoconductivity σ_0, $L_0 = \mu\tau E_0$ is the average drift length of the photoelectrons in the external electric field E_0, $L_D = \sqrt{D\tau} = \sqrt{\mu\tau E_D/K}$ is the average diffusion length, and $E_D = KD/\mu = Kk_BT/q$ is the diffusion field, where D is the diffusion constant and τ is the relaxation time. For lithium niobate, $E_0 = 0$, i.e. no external field is necessarily required as the photovoltaic field plays the dominating role for charge transport and for the index grating formation, and thus, $L_0 = 0$. A steady-state

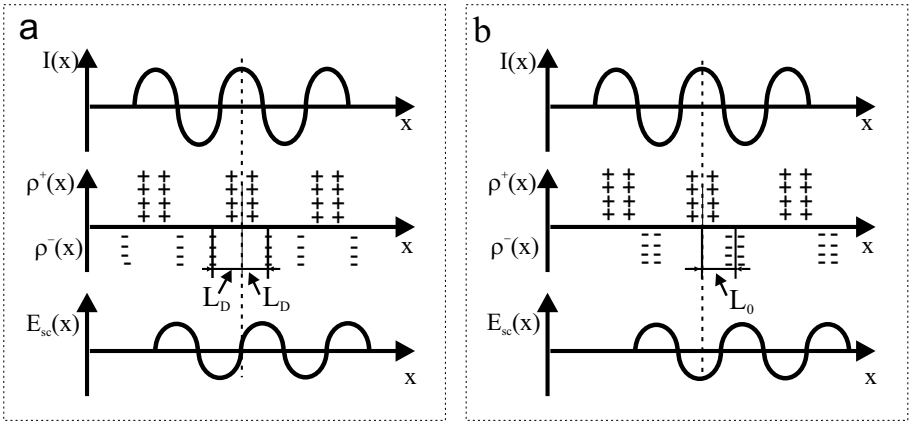

Figure 3.3: Formation of the electric field grating from the spatial distribution of the light intensity by (a) Diffusion mechanism and (b) Drift mechanism.

regime of the hologram recording is a state of the crystal that is continuously illuminated by the interference pattern (eqn (3.14)), when the amplitude of the electric field grating remains constant ($\partial E_{sc}/\partial t = 0$). From eqn. (3.22), the steady-state amplitude of the recorded grating is

$$E_{sc}^{st} = -m(iE_D + E_0 + E_{ph}). \tag{3.23}$$

Analyzing this equation: First, the steady-state hologram amplitude is proportional to the modulation depth of the interference pattern, i.e., the photorefractive crystals can be regarded as "linear" holographic media (only for small light intensity). Second, E_{sc}^{st} proves to be independent of the recording light intensity. The later however is valid only as long as the dark conductivity of the crystal can be ignored in comparison to its photoconductivity.

In the specific case of a crystal with a negligible photovoltaic field and with no external field applied ($E_{ph}, E_0 = 0$), the first term on the right-hand side of the eqn.(3.23) begins to play a dominating role. This is the so-called diffusion mechanism, where the holograms

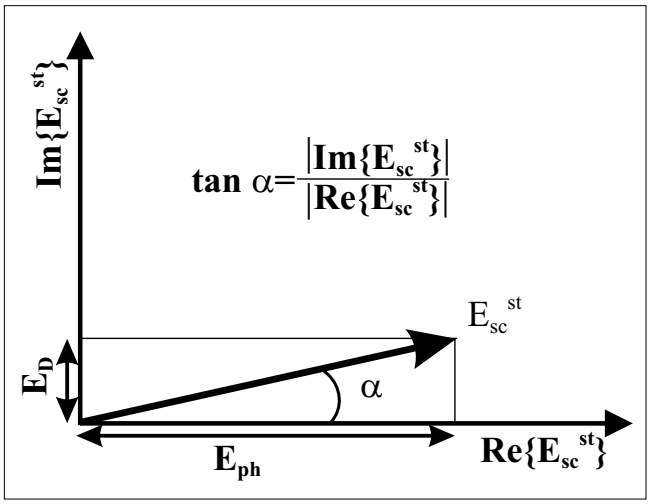

Figure 3.4: Orientation of the steady state space charge field vector in the complex plane (for lithium niobate).

are formed by diffusion of mobile charge carriers from the bright interference fringes to the dark ones. The mechanism is characterized by a linear relationship between the steady-state grating amplitude and the spatial frequency ($E_D = Kk_BT/q$), and also by $\pi/2$ phase shift of the electric field grating $E_{sc}(x)$ from the interference pattern $I(x)$.

In the opposite case, when the photovoltaic field E_{ph} exceeds the diffusion field ($E_{ph} \gg E_D$), or a fairly high external field is applied to the crystal ($E_0 \gg E_D$), the imaginary term on the right-hand side of the eqn. (3.23) can be neglected. This is the so-called drift mechanism of recording. The recording process consists of a partial compensation of the respective field (E_0 or E_{ph}) at the maxima of the recorded pattern $I(x)$. So the steady-state grating produced via the drift mechanism turns out to be unshifted. In the presence of the external field or the photovoltaic field, the change of the index of refraction takes place by two mechanisms: Diffusion and Drift. Diffusion mechanism gives rise to the electric field grating which is shifted by a phase factor of $\pi/2$ from the interference pattern. Drift mechanism gives rise to unshifted grating as shown in Fig. 3.3.

For lithium niobate, the steady state space-charge field is described in complex notation as $E_{sc}^{st} = m(iE_D + E_{ph})$, where E_D is the diffusion field and E_{ph} is the photovoltaic field. For lithium niobate, the photovoltaic field is much larger than the diffusion field. This results in the partial shift of the grating given by the angle α. Fig. 3.4 shows the space-charge field vector in the complex plane and resultant shift (α) of the grating. For $LiNbO_3 : Fe$, E_{ph} ≅50-70 kV/cm in heavily doped samples and E_D =1.6 kV/cm for $\Lambda = 1\mu m$ (at T=300K) [33] and so $\alpha \approx 1.5°$.

Chapter 4

Volume Holographic Lenses and Mirrors

The purpose of this study was to demonstrate electrical control of diffraction from volume holograms recorded using the photorefractive effect. The following chapter contains the details of calculations and considerations to choose the optimal experimental geometry and orientation of the crystal to have the best electrical control of diffraction, description of the experimental set-ups, various components used, results on electrical switching of holographic lenses and holographic mirrors (switching of direction) and estimations of switching time.

4.1 Introduction

Though the introduction to the electrical control of diffraction in photorefractive crystals dates back to 1978-79 [5, 6], the interest in this technique arose again in the nineties with the progress in developing a volume holographic memory and high-selective holographic filters. The electric field multiplexing of volume holograms in $LiNbO_3$ was reported for the first time in 1995 [27], but voltage requirements were quite high at that time. In order to use the electrical control of diffraction for useful applications, it is important to consider the electric field selectivity (EFS). EFS is defined as the specific value of the electric field required to switch the diffraction efficiency of a hologram from maximum to zero or minimum. The lower the EFS, the better it will be to have increased speed of switching and to increase the number of stored or multiplexed holograms. In order to improve the EFS, one has to choose:

1. Optimal experimental geometry-

(a) transmission or reflection geometry for recording and read-out of holograms, whichever gives the high refractive-index or electric field selectivity.

(b) longitudinal or transverse configuration of the electro-optic effect, whichever allows to use lower voltages and still brings appreciable changes in the refractive index.

2. Optimal orientation of the crystal- (orientation of the $\overrightarrow{C}$-axis) to have appreciable grating amplitude as well as better electrical control.

The solution to the first problem could be found in literature. For the second problem, detailed calculation were performed to prepare specific types of crystal with calculated optimum orientation.

4.2 Optimal Experimental Geometry

4.2.1 Recording Geometry and Electric Field Selectivity

The electric field selectivity (EFS) E_{SW} for volume holograms is a specific value of the electric field for which, when applied to the crystal, the diffraction efficiency goes to zero (or minimum) ($\eta(E_{SW}) = 0$). The Bragg condition

$$\Lambda = \frac{\lambda}{2n \sin \Theta_B}, \tag{4.1}$$

is valid only for the case of unlimited dimension of the hologram (or grating) along the direction of light propagation. In practical situations, due to the limited dimensions of the hologram, the Bragg diffraction can be observed over some finite interval of variations of the parameters such as wavelength, angle or refractive index. The rigorous analysis of diffraction efficiency of volume hologram as a function of the angular and wavelength detuning parameters was presented in chapter 2. Here, I will present the analysis of the diffraction efficiency of volume holograms as a function of the refractive index detuning parameter.

In non-centro symmetric crystals, the variation of the refractive index under the influence of an external applied electric field is induced or generated by the combination of three effects: Electro-optic, Photo-elastic and Piezo-electric effects and can be expressed as:

$$\Delta n(E) = -\frac{n^3}{2}(r_{ik}E_k + p_{ij}d_{jk}E_k). \tag{4.2}$$

where, E is the external electric field, r_{ik}, p_{ij} and d_{jk} are components of the Electro-optic, Photo-elastic and Piezo-electric tensors, respectively.

For the case of a high frequency electric field applied to the medium, the second part on the right-hand side in eqn. (4.2) could be neglected. For the case of low frequency or

constant applied electric field, we must take into account all the components. However, at low frequencies, we can introduce a new formulation for the change in the refractive index where we introduce DC electro-optic coefficients, which are considered to take into account the other two components of photo-elastic and piezo-electric coefficients. This new formulation may be given as:

$$\Delta n(E) = -\frac{n^3}{2} r_{ik}^{DC} E_k. \tag{4.3}$$

The applied electric field results not only in variations of the refractive index, but also in sample deformations. This happens because an electro-optic crystal always exhibits the piezoelectric effect. The variations of the grating wave vector, under the influence of an external electric field, can be presented as

$$\frac{\Delta K_g(E)}{K_g} = d_{jk} E_k. \tag{4.4}$$

Fig. 2.1 in chapter 2 presents a general geometry for hologram recording. β is the angle between the normal to the surface of the recording medium and the middle bisector between the incident wave direction ρ and the diffracted wave direction σ and θ_0 is the Bragg angle. Angle $\beta = 0°$, for the case of exactly symmetrical counter-propagation geometry (reflection geometry) of recording and $\beta = 90°$ for symmetrical transmission geometry.

For the non-symmetric holographic recording, the variations of the Bragg angle can be presented in terms of variations in the refractive index using Snell's law as

$$\Delta\theta_0(E) = -\tan(\theta_0 + \beta)\frac{\Delta n(E)}{n}. \tag{4.5}$$

Generally, the variations of the refractive index not only depend on the electric field but also on the wavelength. So one can write

$$\Delta n(E, \lambda) = \Delta n(E) + \frac{dn}{d\lambda}\Delta\lambda. \tag{4.6}$$

Differentiating eqn. (4.1) yields

$$\frac{\Delta\lambda}{\lambda} \approx \frac{\Delta n(E, \lambda)}{n} + \frac{\Delta K_g(E)}{K_g} + \Delta\theta_0(E) \cdot \cot\theta_0. \tag{4.7}$$

Inserting eqns (4.5) and (4.6) into eqn. (4.7) yields the final expression describing the relation between the spectral selectivity and the variations of the refractive index under the influence of the external electric field and this is presented as

$$\frac{\Delta\lambda}{\lambda} \approx \frac{\Delta n(E)/n[1 - \tan(\theta_0 + \beta) \cdot \cot\theta_0] + d_{jk}E_k}{\left[1 - \frac{dn}{d\lambda} \cdot \frac{\lambda}{n}[1 - \tan(\theta_0 + \beta) \cdot \cot\theta_0]\right]}. \tag{4.8}$$

The dispersion ($dn/d\lambda$) can be neglected in comparison to the ratio between wavelength and refractive index ($dn/d\lambda \ll \lambda/n$). For example, for $\lambda = 532nm$, $(\frac{dn}{d\lambda} \cdot \frac{\lambda}{n}) \approx 0.1$ for lithium niobate.

Furthermore, for lithium niobate, the piezoelectric coefficients $\approx 10^{-11}$. This implies variations of the grating period is given by, $\Delta\Lambda/\Lambda \approx 10^{-5}$. At the same time, the variations of the refractive index due to the electro-optic effect, $\Delta n/n \approx 10^{-4}$. So, the influence of the piezo-electric effect is $< 10\%$ and thus, the component containing piezo-electric coefficients ($d_{jk}E_k$) can be neglected.

Taking into account all these simplification results in

$$\frac{\Delta\lambda}{\lambda} = \frac{\Delta n(E)}{n}[1 - \cot\theta_0 \tan(\theta_0 + \beta)]. \tag{4.9}$$

This equation gives the relation between the spectral selectivity and the selectivity of the refractive index. Using the relation for the wavelength selectivity (eqn. (2.39), chapter 2) as given in coupled-wave theory, the refractive index selectivity in the perfect reflection geometry ($\theta_0 = 90°$ and $\beta = 0°$) can be obtained as

$$\frac{\Delta n}{n} = \frac{\Lambda}{T}. \tag{4.10}$$

Using the above equation, the detuning parameter (eqn. (2.38)) can be defined as $\xi_r = -\frac{\Delta n}{n}\beta T \sin\theta_0$. Using this detuning parameter and eqn. (2.36), a theoretical plot is obtained for the diffraction efficiency as a function of the detuning parameter. From Fig. 4.1, one

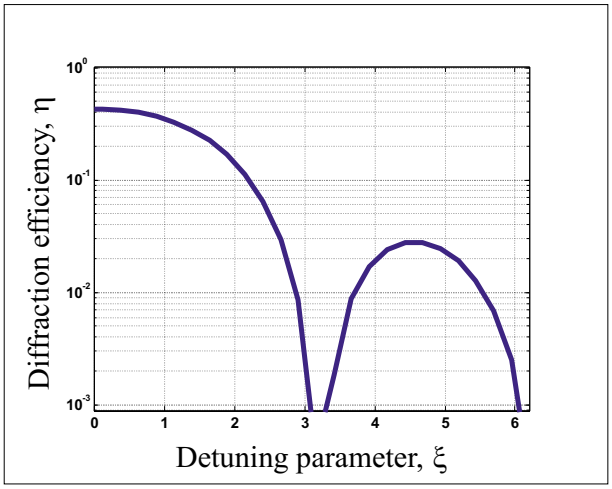

Figure 4.1: Theoretical plot for dependence of the diffraction efficiency on the detuning parameter.

can obtain a value of the detuning parameter, for which the diffraction efficiency reaches its

first minimum. Using eqns. (4.3) and (4.10), an expression for the electric field selectivity of volume reflection holograms can be obtained as

$$E_{SW} = \frac{2\Lambda}{n^2 T r_{eff}^{DC}}. \tag{4.11}$$

where, T is the thickness of the hologram, Λ is the grating period and r_{eff}^{DC} is the effective electro-optic coefficient. This coefficient allows to take into account the anisotropy of the crystal. From the presented analysis and specially from eqn. (4.11), it can be seen that to achieve the highest possible electric field selectivity (lowest possible voltage, required to bring diffraction efficiency from maximum to zero), the grating period should be as small as possible and the thickness T of the hologram as large as possible. So, in order to achieve higher selectivity, a symmetrical reflection geometry should be used for recording and the largest possible thickness of the hologram should be used. From the same eqn.(4.11), it can be seen that an external electric field could be used for multiplexing a number of holograms in the same volume. The maximum possible number of holograms (M), that can be multiplexed electrically, could be estimated as

$$M = 2\frac{E_{BD}}{E_{SW}}. \tag{4.12}$$

where E_{BD} is the breakdown electric field (generally $E_{BD} \cong 30kV/cm$). The factor 2 appears as we can use both the positive and negative polarities of the electric field.

4.2.2 Optimal Configuration of the Electro-optic Effect

In **transverse configuration** of the electro-optic effect, the light beam propagates perpendicular to the direction of the applied electric field. The advantage of this configuration (as shown in Fig. 4.2) is that the electrodes do not obstruct the optical beam unlike in longitudinal geometry. As it will be seen that for this configuration, the retardation is proportional to the applied voltage and also to the length of the crystal and thus the half-wave voltage is proportional to the ratio (d/T) of the width of the crystal to its length. Thus, by decreasing this ratio, one can reduce the half-wave voltage. The half-wave voltage can be expressed as

$$V_\pi = \frac{\lambda}{n^3 r_{eff}} \left(\frac{d}{T}\right) \tag{4.13}$$

where, d is the thickness of the crystal and T is the length of the crystal along the direction of propagation of light beam. In order to obtain the order of magnitude of the half-wave voltage required, I consider a lithium niobate crystal having the following specifications:

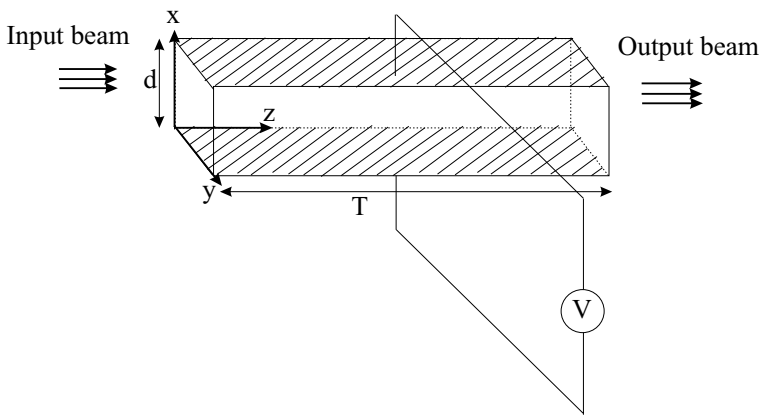

Figure 4.2: The transverse configuration of the electro-optic effect

$d = 2.5mm$ and $T = 10mm$. Let $\lambda = 532nm$ and $n_e = 2.23$ for lithium niobate at 532nm wavelength. We consider the effective electro-optic coefficient as $r_{33} = 30.8pm/V$. For all these parameters, the half-wave voltage comes out to be approximately 390 Volts, which is much lesser as compared to a few kilovolts required in the longitudinal geometry. This value can further be reduced by choosing a lower value of d/T ratio. Lower voltages and hence faster switching is possible with transverse configuration and hence this configuration was chosen for my experiments.

4.3 Optimal Orientation of the Crystal

In this section, the dependence of the electric field selectivity (EFS) on the orientation of the crystal will be checked. The analysis begins with the general orientation of the crystal as shown in Fig. 4.3. For photorefractive crystals both the refractive index variation (Δn) and the grating amplitude (n_1) are dependent on the mutual orientation of the principal axes, the external electric field, the space-charge field and the vector of light polarization [44]. To solve the equation for the optical indicatrix at an arbitrary crystal orientation, a detailed theoretical analysis was performed. The aim was to find the dependence of the cross-section of the optical indicatrix on the external electric field.

4.3.1 Dependence of EFS on the Orientation of the Crystal

The arbitrary orientation of the crystal can be presented from three independent angles of rotation of the principal crystallographic axes relative to the chosen system of coordinates. Angle α is the angle between the optical $\overrightarrow{C}$-axis and the plane which is normal to the direction of propagation of the read-out beam. Angle β is the angle between the z-axis and

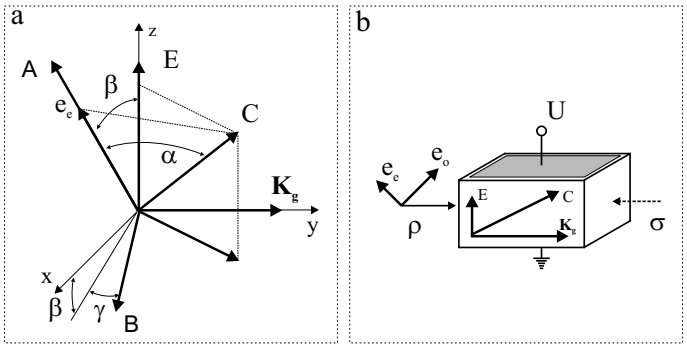

Figure 4.3: (a) General orientation of various vectors, (b) Orientation of the crystal w.r.t. recording beams and applied electric field

the projection of the c-axis in the plane perpendicular to the direction of propagation of light (this angle gives the orientation of the e-o polarization). Angle γ is the angle of the rotation around the c-axis. Taking into account these transformations, the transformation matrix can be written as

$$\hat{f} = \hat{\gamma} \cdot \hat{\alpha} \cdot \hat{\beta} = \begin{pmatrix} a & b & c \\ d & e & f \\ g & h & i \end{pmatrix} \tag{4.14}$$

where,

$$\hat{\alpha} = \begin{pmatrix} 1 & 0 & 0 \\ 0 & \cos\alpha & -\sin\alpha \\ 0 & \sin\alpha & \cos\alpha \end{pmatrix}, \hat{\beta} = \begin{pmatrix} \cos\beta & 0 & -\sin\beta \\ 0 & 1 & 0 \\ \sin\beta & 0 & \cos\beta \end{pmatrix}, \hat{\gamma} = \begin{pmatrix} \cos\gamma & -\sin\gamma & 0 \\ \sin\gamma & \cos\gamma & 0 \\ 0 & 0 & 1 \end{pmatrix} \tag{4.15}$$

Taking the transformations defined by eqn. (4.14) and considering the electro-optic tensor of crystals belonging to point group symmetry 3m, the equation of optical indicatrix can be written as

$$\begin{aligned} &\left[\frac{1}{n_0^2} + (r_{13}i - r_{22}f)E\right](ax+by+cz)^2 + \left[\frac{1}{n_0^2} + (r_{13}i + r_{22}f)E\right](dx+ey+fz)^2 \\ &+ \left[\frac{1}{n_e^2} + r_{33}iE\right](gx+hy+iz)^2 + 2(dx+ey+fz)(gx+hy+iz)fr_{51}E \\ &+ 2(ax+by+cz)(gx+hy+iz)cr_{51}E - 2(ax+by+cz)(dx+ey+fz)cr_{22}E = 1 \end{aligned} \tag{4.16}$$

which in the simplified form can be written as

$$\left(\frac{1}{n_0^2} + AE\right)x'^2 + \left(\frac{1}{n_0^2}\sin^2\alpha + \frac{1}{n_e^2}\cos^2\alpha + BE\right)z'^2 + Cx'z'E = 1 \tag{4.17}$$

where x' and z' are the transformed co-ordinates, E is the external electric field and n_o and n_e are ordinary and extra-ordinary refractive indices. To find the variations of the

refractive indices, the index ellipsoid is cut along a plane perpendicular to the direction of propagation ($\overrightarrow{\rho}$) of the read-out beam and this cross-section of the optical indicatrix has the form of an ellipse as shown in Fig. 4.4, where its axes give the orientation of ordinary and extra-ordinary polarization directions and the length of its principal axes gives the value of the ordinary and extra-ordinary refractive indices. The equation describing this ellipse is given in eqn. (4.17).

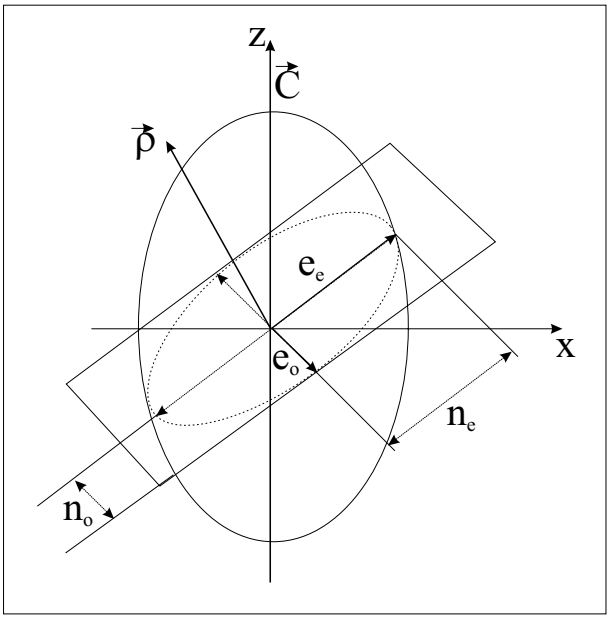

Figure 4.4: Intersection curve of a plane normal to the direction of propagation and the index ellipsoid

Coefficients A, B, and C describe the deformations of the optical indicatrix under the influence of an external electric field and are given as

$$\begin{aligned}
A &= r_{13}\cos\alpha\cos\beta \\
&+ r_{22}[3\sin\gamma\cos\gamma(\sin\beta\cos\gamma - \sin\alpha\cos\beta\sin\gamma) \\
&+ \sin\alpha\cos\beta\cos\gamma - \sin\beta\sin^3\gamma] \\
B &= \cos\alpha\cos\beta[r_{13}\sin^2\alpha + r_{33}\cos^2\alpha + 2r_{51}\sin^2\alpha] \\
&- r_{22}\sin^2\alpha[3\sin\alpha\cos\gamma(\sin\beta\cos\gamma - \sin\alpha\cos\beta\sin\gamma) \\
&+ \sin\alpha\cos\beta\cos\gamma - \sin\beta\sin^3\gamma] \\
C &= -2r_{51}\cos\alpha\sin\beta \\
&- 2r_{22}\sin\alpha[\sin\beta\cos^3\gamma + \sin\alpha\cos\beta\sin^3\gamma \\
&- 3\sin\gamma\cos\gamma(\sin\beta\sin\gamma + \sin\alpha\cos\beta\cos\gamma)].
\end{aligned} \tag{4.18}$$

This analysis is general and can be applied to all crystals in group symmetry 3m and also with some special conditions, to crystals within point group 4mm. The analysis may be the same but final optimal orientation will differ from crystal to crystal.

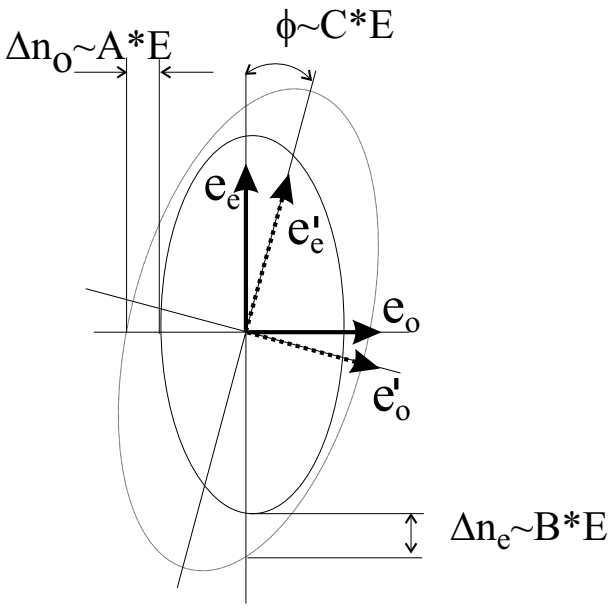

Figure 4.5: Influence of the external electric field on the cross-section of the optical indicatrix

Fig. 4.5 describes the deformation of the index-ellipsoid due to three factors, A, B, and C. Coefficients A and B describe variations of the refractive indices for ordinary and extra-ordinary polarizations given as

$$\Delta n_o \approx \frac{1}{2} n_o^3 A E \tag{4.19}$$

and

$$\Delta n_e \approx \frac{1}{2} \left(\frac{n_e n_o}{\sqrt{n_e^2 \sin^2 \alpha + n_o^2 \cos^2 \alpha}} \right)^3 B E. \tag{4.20}$$

The coefficient C describes the angle of rotation of the ellipsoid given as

$$\phi \approx \frac{1}{2} \cdot \frac{C n_e^2 n_o^2 E}{\cos^2 \alpha (n_e^2 - n_o^2)}. \tag{4.21}$$

For the particular case of the crystal orientation, where $\beta = 0, \gamma = 0$, coefficients A and B are obtained as

$$\begin{aligned} A(\alpha) &= r_{13} \cos \alpha + r_{22} \sin \alpha \\ B(\alpha) &= r_{13} \cos \alpha \sin^2 \alpha + r_{33} \cos^3 \alpha + 2 r_{51} \cos \alpha \sin^2 \alpha - r_{22} \sin^3 \alpha. \end{aligned} \tag{4.22}$$

Both A and B are functions of parameter α, so the variations of the ordinary and extra-ordinary refractive indices as given in eqns. (4.19) and (4.20) can also be presented as

functions of angle α. A and B can be treated as effective electro-optic coefficients for ordinary and extra-ordinary polarizations, respectively. These can be plotted as a function of angle α as shown in Fig. 4.6.

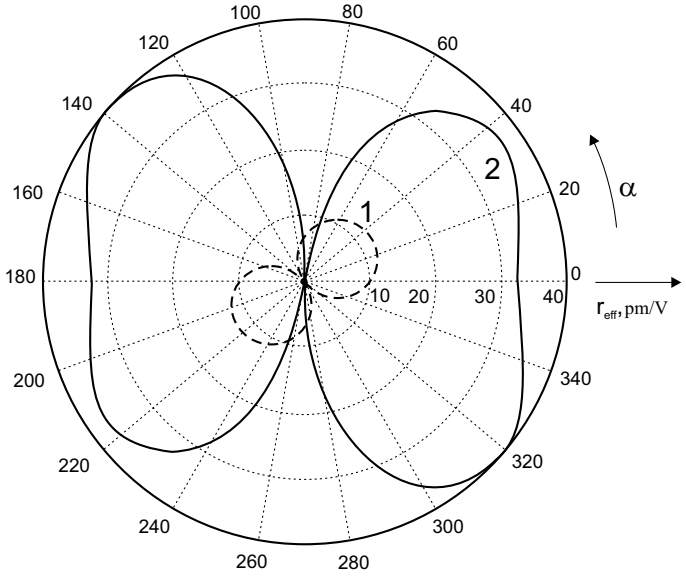

Figure 4.6: Theoretical plots for effective electro-optic coefficients for ordinary (1) and extra-ordinary (2) polarization.

From Fig. 4.6, the behavior of A and B can be seen with angle α. From this plot, a particular value of angle α can be chosen, which gives maximum possible value of A and B. This plot shows that the effective electro-optic coefficient for ordinary polarization (A) is very small for all possible values of angle α. This fact leads us to use extra-ordinary polarization for better electrical control as the corresponding effective electro-optic coefficient (B) is much larger than that of ordinary polarization.

From Fig. 4.6, we see that the maximum effective electro-optic coefficient for extra-ordinary polarization is obtained near $\alpha = -40°$. About $\alpha = +40°$ also, one can obtain good enough value for the coefficient. But effective electro-optic coefficient is not the sole factor determining electric-field selectivity. Other factors should also be considered, before choosing an optimum value for angle α.

4.3.2 Dependence of EFS on the Grating Amplitude.

It is known for the case of wavelength and angular selectivities that they depend on the grating amplitude. In a similar way, the electric field selectivity may also depend on the grating amplitude. The diffraction efficiency of reflection volume holograms can be

presented as a combination of two parameters as

$$\eta = \frac{1}{\left(\frac{\xi_r}{\nu_r}\right)^2 + \left[1 - \left(\frac{\xi_r}{\nu_r}\right)^2\right] \coth^2 \sqrt{\nu_r^2 - \xi_r^2}}. \tag{4.23}$$

Here, ξ_r is the detuning parameter and it could be presented as a function of wavelength variations, angular variations and for the case of electrical field selectivity, it can also be presented in terms of refractive index variations as [25]

$$\xi_r = \frac{2\pi}{\lambda} nT \frac{\Delta n(E)}{n}. \tag{4.24}$$

The second parameter is ν_r and it depends on the grating amplitude as

$$\nu_r = \frac{\pi n_1 T}{\lambda}. \tag{4.25}$$

ξ_r and ν_r play an equivalent role to determine the diffraction efficiency and selectivity. Eqns. (4.24) and (4.25) suggest that the selectivity depends also on the grating amplitude, n_1. If the grating amplitude is very small ($n_1/n \ll 1$), the intensity of light at the input face and at the output face of the crystal (hologram) will be almost the same as the diffraction efficiency will be very small for such a case. In this case, the whole grating over the hologram thickness T contributes and behaves in the similar way throughout. If the grating amplitude is very high ($n_1/n \gg 1$), there will be a very high diffraction efficiency too and for such a case, it may happen that only a certain initial part of the grating diffracts the entire light and only a very small part of incident beam may reach the rest of the grating. In this case the grating is effective not over the entire thickness of hologram. So the behavior of the rest of the grating will be different and this may affect the diffraction efficiency. So, one has to always consider the grating amplitude while calculating the dependence of selectivity.

For large grating amplitudes, the wavelength selectivity can be estimated as [45].

$$\frac{\Delta\lambda}{\lambda} = \frac{n_1}{2n}. \tag{4.26}$$

From Eqn. (4.26) and using $\Delta n/n = \Delta\lambda/\lambda$ and Eqn. (2.39), the approximate relation can be deduced

$$\frac{\Delta n}{n} = \frac{n_1}{2n} \approx \frac{\Lambda}{T} \tag{4.27}$$

and from this equation, it can be seen that the electric field selectivity depends on the grating amplitude.

4.3.3 Dependence of the Grating Amplitude on the Crystal Orientation.

We will consider the steady state case of a holographic grating. The grating amplitude can be calculated from the amplitude of the space-charge electric field, E_{SC} and the effective electro-optic coefficient, r_{eff}, which depends on the crystal orientation and the direction of the space charge electric field as given in

$$n_1 = \frac{1}{2} n^3 r_{eff}(\alpha) E_{SC} \tag{4.28}$$

where α is the angle between the $\overrightarrow{C} - axis$ and the applied electric field. For simplicity, we suppose, angles $\beta = 0$ and $\gamma = 0$. We also assume that the incident light distribution (interference pattern) responsible for grating formation, has a sinusoidal spatial variation along y-axis only.

$$I(y) = I_0 \cos(K_g y) \tag{4.29}$$

The amplitude of the space charge field could be calculated from Maxwell's equations

$$\begin{aligned} div\,\overrightarrow{E}_{SC} &= \frac{\partial \overrightarrow{E}_{SC}}{\partial y} = \frac{\rho(y)}{\varepsilon} \\ rot\,\overrightarrow{E}_{SC} &= 0 \end{aligned} \tag{4.30}$$

The distribution of the space-charge field density ρ has the same profile as of the interference pattern (eqn. 4.29)) but with some phase shift ϕ (due to photorefractive effect) as can be seen in

$$\rho(y) = \partial\rho \cos(K_g y + \phi) \tag{4.31}$$

In this case, the components of the space charge field can be calculated using eqns. (4.30) and (4.31) and can be presented as

$$\begin{aligned} E_b^{SC} &= \frac{\partial\rho}{|K_g|(\varepsilon_a \cos^2\alpha + \varepsilon_c \sin^2\alpha)} \cos\alpha \\ E_c^{SC} &= \frac{\partial\rho}{|K_g|(\varepsilon_a \cos^2\alpha + \varepsilon_c \sin^2\alpha)} \sin\alpha \end{aligned} \tag{4.32}$$

where E_c is the projection of the space-charge field on the C-axis and E_b is the projection of the field on an axis perpendicular to the C-axis, in the same plane. From the introduction

to theory of photorefractives (chapter 3) it is known that the maximum possible amplitude or the charge density is limited by the efficient trap concentration as

$$\partial\rho \approx qN_A. \tag{4.33}$$

From this, one can define the value and the direction of the space-charge field. Now,

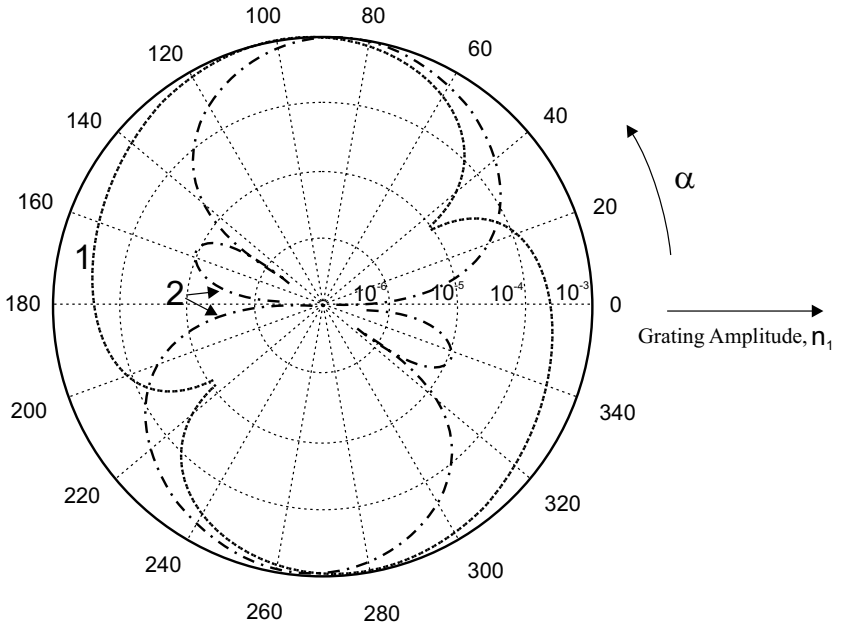

Figure 4.7: Theoretical plots for dependence of grating amplitude on the angle α, for ordinary (1) and extra-ordinary (2) polarization.

the variations of the refractive index under the influence of the space-charge electric field can be calculated. For this particular problem, the equation of the optical indicatrix in standard system of co-ordinates will be used

$$\begin{aligned}&\left(\frac{1}{n_o^2} - r_{22}E_b^{SC} + r_{13}E_c^{SC}\right)x^2 + \left(\frac{1}{n_o^2} + r_{22}E_b^{SC} + r_{13}E_c^{SC}\right)y^2 \\ &+ \left(\frac{1}{n_e^2} + r_{33}E_c^{SC}\right)z^2 + 2yzr_{51}E_b^{SC} = 1.\end{aligned} \tag{4.34}$$

The cross section of the optical indicatrix can be found by cutting it with the plane normal to the propagation vector of the read-out light (Fig. 4.4). Eigenvectors for ordinary and extra-ordinary wave polarizations can be written as

$$e_e = \begin{pmatrix} 0 \\ -\sin\alpha \\ \cos\alpha \end{pmatrix}; e_o = \begin{pmatrix} 1 \\ 0 \\ 0 \end{pmatrix}. \tag{4.35}$$

Repeating the same process as in section 4.3.1, the variations of the ordinary and extra-ordinary refractive indices due to the space-charge field can be obtained. These variations are nothing but the grating amplitudes for ordinary and extra-ordinary polarizations as shown in Fig. 4.7 (for the parameters: $N_A = 10^{18} cm^{-3}$, $\lambda = 633nm$ and $T = 1cm$). A dependence on angle α for the grating amplitude is obtained as shown in the following equation

$$
\begin{aligned}
n_1^o &= -\frac{1}{2} n_0^3 \frac{qN_A}{|K_g|(\varepsilon_a \cos^2\alpha + \varepsilon_c \sin^2\alpha)} (r_{13}\sin\alpha - r_{22}\cos\alpha) \\
n_1^e &= -\frac{1}{2} \left(\frac{n_o n_e}{\sqrt{n_e^2 \sin^2\alpha + n_o^2 \cos^2\alpha}} \right)^3 \frac{qN_A}{|K_g|(\varepsilon_a \cos^2\alpha + \varepsilon_c \sin^2\alpha)} \times \\
&\times (r_{13}\sin^3\alpha + r_{33}\sin\alpha\cos^2\alpha + r_{22}\sin^2\alpha\cos\alpha - r_{51}\sin\alpha\cos^2\alpha).
\end{aligned}
\tag{4.36}
$$

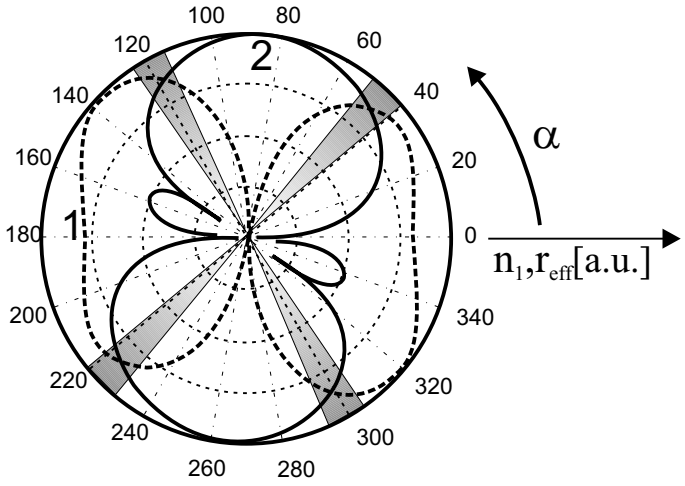

Figure 4.8: Theoretical plots for the dependence of the effective electro-optic coefficient (1) and the grating amplitude (2) on the angle α, for extra-ordinary polarization.

From Fig. 4.7, it can be seen that the maximum grating amplitude for extra-ordinary polarization is obtainable near $\alpha = 90°$ i.e. when $\overrightarrow{K}_g \parallel \overrightarrow{C}$, which is conventional crystal orientation for recording reflection holograms, but the electro-optic coefficient is almost zero for this value of angle α. Here arises a conflicting situation, as the maximum effective electro-optic coefficient is obtained near $\alpha = +40°$ or near $\alpha = -40°$. The effective electro-optic coefficient is the parameter deciding electric field selectivity and the grating amplitude is the parameter deciding the diffraction efficiency. Both parameters depend on angle α and so one has to make a compromise while choosing an optimum value for α. Comparing the Figs. 4.6 and 4.7, we can find a compromising orientation of the crystal and this orientation will give acceptable electric field selectivity and acceptable grating amplitude.

For this purpose, one can multiply the two parameters and then find out the maxima of this multiplied function. Fig. 4.8 shows the behavior of the effective electro-optic coefficient and the grating amplitude as function of angle α. The darkened stripes show the region of maxima of the multiplied function. One can choose a value of the angle α in this range and that will be the optimum value. So, based on the entire analysis, the optimal range for angle α was between $40° - 50°$. One gets appreciable diffraction efficiency and effective electrical control for α in this optimal range.

Based on the above analysis, various critical parameters taken into consideration for experimental investigations are

1. Reflection recording geometry and larger length of crystals ($T = 10mm$ to have better electric field selectivity).

2. Transverse electro-optic effect to reduce the voltage requirements.

3. $\alpha = 45°$ (The angle between the $\overrightarrow{C}$-axis and the applied electric field), to have best compromise between diffraction efficiency and electric field selectivity.

Incorporating all the above factors, basic measurements were done to have an estimation of electric field selectivity (EFS) with the optimized set-up. In the following sections, all the measurements and the results are compiled.

4.4 Basic Experimental Set-up

The basic experimental setup for the investigations of electrical control of diffraction is shown in Fig. 4.9. An Nd:YAG cw laser @$\lambda = 532$ nm with $I = 100mW$ output power was used. The plane wave obtained after the beam expander assembly, was split into two beams: σ and ρ . The $LiNbO_3$ crystal was illuminated from the opposite sides by recording beams σ and ρ . In this case the Bragg angle Θ_B was approximately $89°30'$. Using a set of neutral density filters, the power of the recording beams could be varied. Time of recording was about 8 minutes for recording beams each with $\approx 200\ \mu W$ intensity. After recording of a hologram, the beam σ was blocked and the reconstructed beam σ_0 is detected by a photodiode or a CCD camera. By applying different electric fields $\overrightarrow{E}$ to the crystal, the dependence of the diffraction efficiency was measured as shown in Fig. 4.11. The dimensions of the iron doped $LiNbO_3$ crystals used are 10 mm x 8 mm x d mm, where $d = 1, 1.5, 2.5$ and 5, as four crystals with different d/T ratio were used. The concentration of Fe^{2+} in all the crystals was 0.05 mol %. The pair of electrodes was attached on the top and bottom surfaces (parallel to the light propagation), the distance between the electrodes was d mm ($d = 1, 1.5, 2.5$ or 5). Fig. 4.10 shows the exact orientation of the crystal as used in the experiments.

In the initial part of the work, holograms of a plane wave were recorded for the calibration of the system. The obtained behavior of diffraction efficiency as a function of the applied

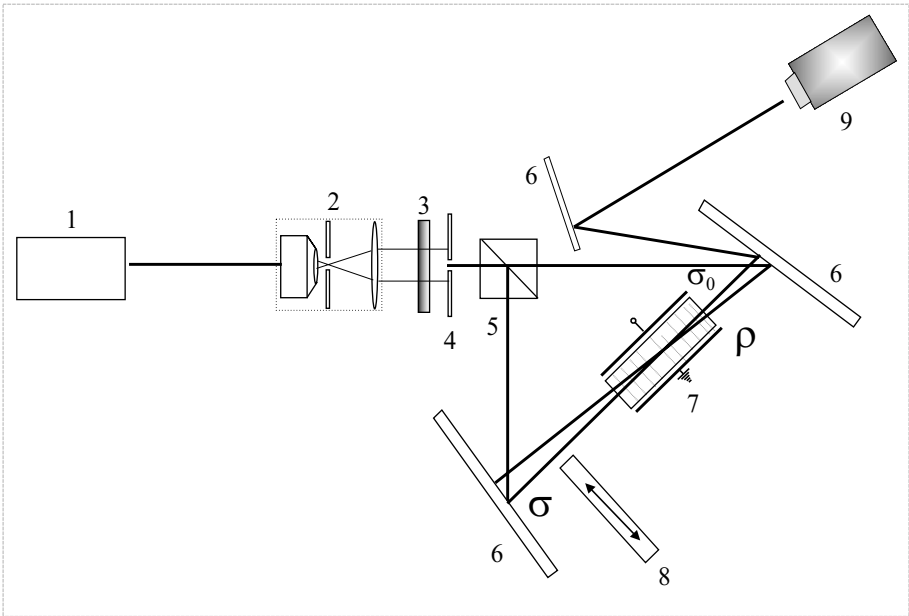

Figure 4.9: The experimental set-up, 1- Nd:YAG cw laser, λ=532 nm , 2 - beam expander, 3 - polarizer, 4 - diaphragm, 5 - beam splitter, 6 - mirror, 7 - crystal with electrodes, 8 - shutter, 9 - photodiode or CCD camera.

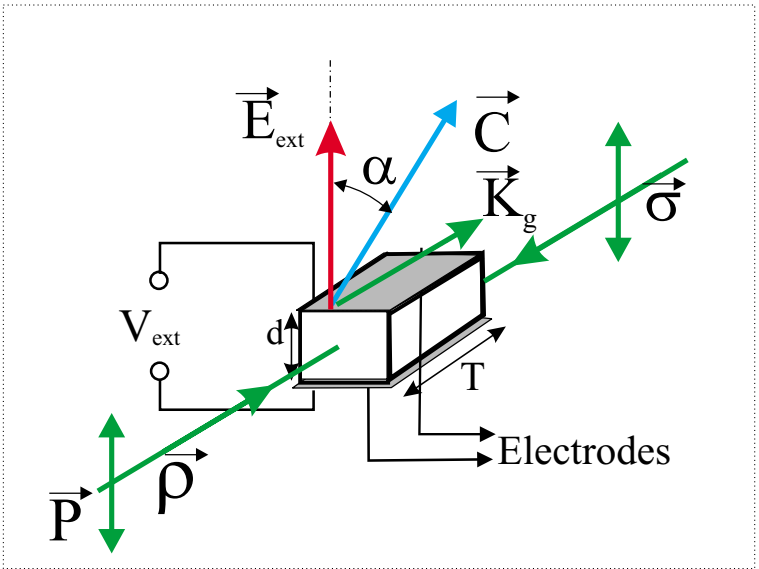

Figure 4.10: Orientation of the $LiNbO_3$ crystal in the experiment: $\vec{\sigma}$ and $\vec{\rho}$ are the propagation vectors of the recording beams, α is the angle between the optical axis$\vec{C}$ and the applied electric field,$\vec{P}$ is the orientation of the wave polarization, $\vec{E}_{ext}$ is the external electric field, T is the thickness of the crystal.

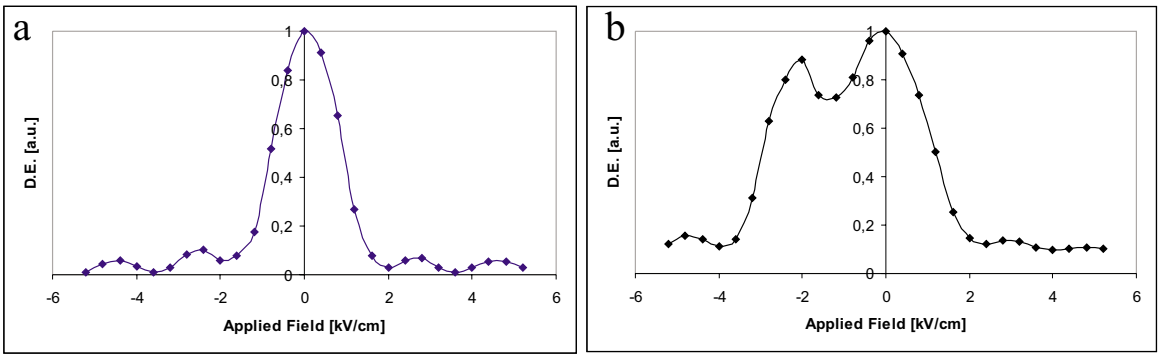

Figure 4.11: Diffraction efficiency of the hologram as a function of the applied field for, (a) one hologram of a plane wave recorded at $E_{ext} = 0$ and (b) two holograms of a plane wave, one recorded at $E_{ext} = 0$ and the other at $E_{ext} = -2kV/cm$.

field is shown in Fig. 4.11 (a). The experimentally obtained dependence was compared with the theoretical plot (obtained using eqn. (4.23)). Fig. 4.12 shows the comparison of the experimental and theoretical plots for dependence of diffraction efficiency on the external field. The diffraction efficiency reaches its first minimum at about $\pm 2kV/cm$ for the hologram of a plane wave. Then multiplexing was done according to the Rayleigh's criteria i.e. the second hologram was recorded at a value of the electric field at which the diffraction efficiency of the first hologram reaches its first minimum as shown in Fig.

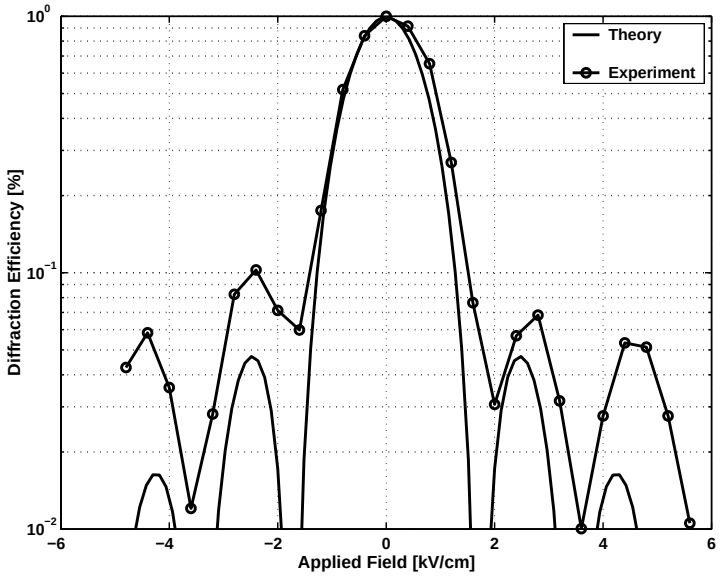

Figure 4.12: Diffraction efficiency of the hologram of a plane wave as a function of the applied field for the theoretical (calculated using eqn. (4.23)) and the experimental data.

4.11 (b). The first hologram was recorded without application of field and the second hologram was recorded at -2kV/cm (EFS). The time of recording and other recording parameters have to be optimized to have both holograms with equal diffraction efficiency. The absolute value of diffraction efficiency for all experiments was between 1-5 %. The decrease of diffraction efficiency between the multiplexed holograms is approximately 25 %, which is quite close to the theoretical limit.

To have an idea of the actual voltage required for crystals with different d/T ratios, the dependence of diffraction efficiency on the applied field was measured for four crystals with different d, in similar manner as explained above and get the plots shown in Fig. 4.13. It can be clearly seen from Fig 4.13 that the crystal with lowest d/T ratio requires the least voltage (see Sec. 4.3) for a complete switching of the hologram.

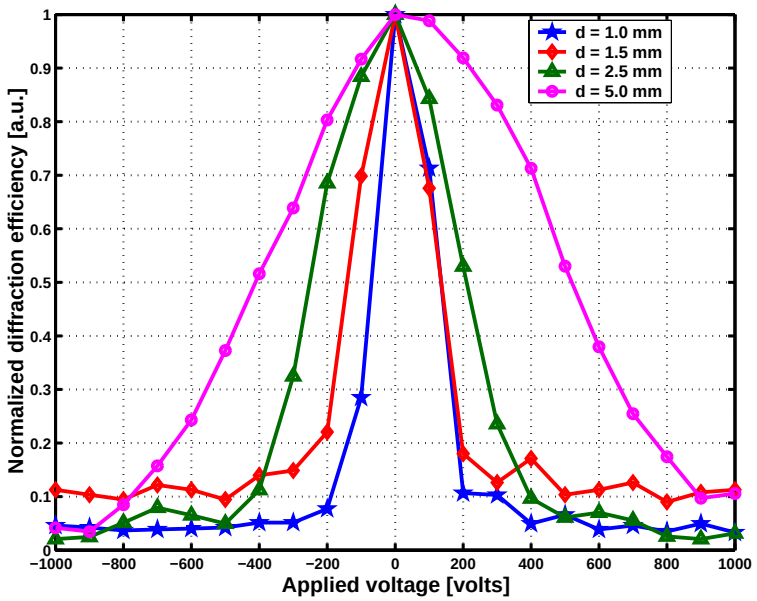

Figure 4.13: Dependence of diffraction efficiency on applied voltage for crystals with different thickness d.

4.5 Holographic Lenses

The term holographic lens stands for a hologram of a lens. This holographic lens functions in the same way as the optical lens as it will have the same focal length as of the lens whose hologram has been recorded. Multiplexing two or more holograms of lenses of different focal lengths in the same volume resembles a holographic lens with variable focal length. Such a lens is very useful for practical applications, provided the switching of focal length is smooth and fast. Therefore, we used electrical switching which offers a switching time of the order

of few micro-seconds. Such a system is competitive with liquid-crystal lenses, made of a layer of nematic liquid crystal with modified planar electrodes around the edge that allow control of the spatial distribution of the electric field within the device. Changing the amplitude and frequency of the drive signal, achieved by the custom-built control electronics, varies the refractive index profile in the crystal and provide the mechanism that produces optical lensing effects and wavefront control. Such lenses with variable focal length have been reported by researchers at the Scots firm CRL Opto and at Durham University [46]. They have developed both spherical and cylindrical liquid crystal lenses with diameters as large as 10 mm, operational wavelengths >400 nm, and a 0 to 2 diopter value that allows them to focus a parallel beam of light between 50 cm and infinity at a switching speed of 1 s [47]. However, demonstrated here are holographic lenses in lithium niobate crystal with electrical control which allows them to focus between 40 cm and 60 cm at a switching speed of about 100 μs. The advantages are fast switching and simple realization as no control over the spatial distribution of the lenses is required as in case of liquid crystal lenses.

These lenses are expected to find use in applications such as focusing and laser beam control and reading/writing of holographic discs.

4.5.1 Experimental Procedure

For the recording of the hologram of a lens, I used the same experimental set-up (Fig. 4.9) as was used for recording the hologram of plane waves, now, with the lens to be recorded, in the path of the signal beam. The part of the set-up (with the lens) used for recording is shown in Fig. 4.14. The experimental procedure for measuring the dependence of diffraction efficiency on the applied field is the same as explained in section 4.4. The only difference is that in this case the CCD camera or photodetector is placed at a distance equal to the focal length of the lens (whose hologram is recorded), from the read-out face of the crystal. This was done to have pictures of focal distribution with the CCD camera and also to control the behavior of the diffraction efficiency in the reconstructed focal plane of the lens. Two achromatic lenses with focal lengths of 40cm and 60cm, respectively, were used for recording. A lithium niobate crystal with 2.5 mm thickness (distance between the electrodes) was used and the beam diameter was about 2 mm. Fig. 4.15 (a) and (b) show the dependence of the diffraction efficiency for the two holographic lenses respectively. Both these holograms were recorded without application of the field to the crystal. The absolute value of the diffraction efficiency was near 1%. Higher values of diffraction efficiency could not be obtained. This can be explained as the crystals were not sufficiently doped and they were not very sensitive. Also, in general, one can go on increasing the recording time to get better diffraction efficiency. However, the reflection geometry is very sensitive to vibrations easily causing disturbance during the recording process. This phenomenon, when a little vibration depletes the grating, was observed many times during recording. Other factors responsible for low diffraction efficiency are large absorption within the crystal and reflections from the polished faces of the crystal. However, the aim was not to achieve very

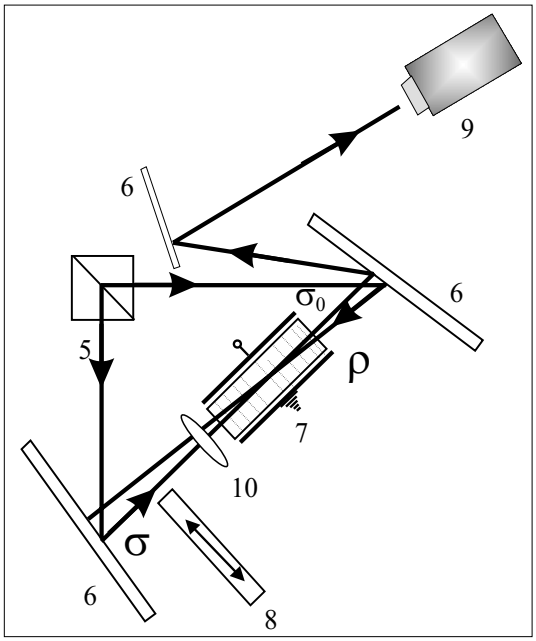

Figure 4.14: Experimental set-up for recording and read-out of the hologram of a lens (part of Fig. 4.9 with one additional component 10- Lens to be recorded).

high efficiency but rather to test the electrical control for switching the focal length, so the diffraction efficiency between 1-5% was sufficient.

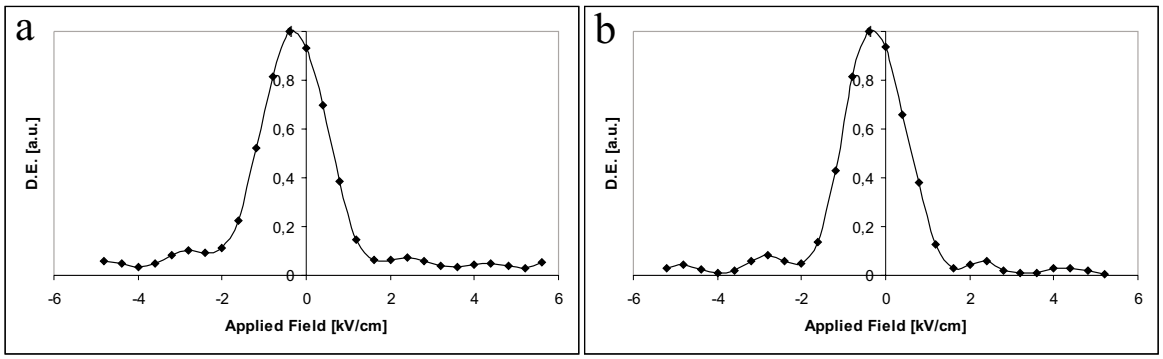

Figure 4.15: Dependence of diffraction efficiency on the applied field for holographic lens with focal length (a) 40cm and (b) 60 cm.

As can be seen from Fig. 4.15, EFS is about $\pm 2kV/cm$, which is similar to the case of holograms of plane waves. To switch off the hologram of a lens, one requires an applied field equal to $\pm 2kV/cm$ and the next holographic lens can be recorded at this value. The shift of the peak of diffraction efficiency is attributed to the photovoltaic field, which arises due

to charge separation caused by non-homogenous illumination of the crystal. Photovoltaic fields are generally very high for lithium niobate crystals (see Sec. 3.4).

The experimental results were compared with the theory (using eqn. (4.23)) for the case of holographic lenses as well and the result is shown in Fig. 4.16 again showing a good match between theory and experimental results for EFS. The large height of side lobes and the non-zero minimum diffraction efficiency, for experimental curve is due to the background noise signal. The explanation for this fact is that the input beam is not 100% linearly polarized and so components of the other polarization also exist. These components are still diffracted and give rise to background signal even when the extra-ordinary polarization reaches minimum diffraction efficiency.

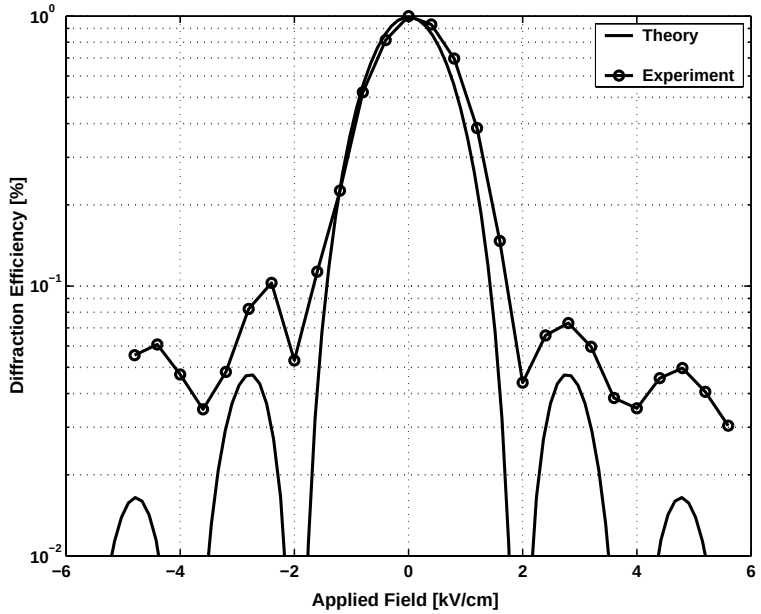

Figure 4.16: Diffraction efficiency of the hologram of a lens as a function of the applied field for theoretical (calculated using eqn. (4.23)) and experimental data.

4.5.2 Electrical Switching of Holographic Lenses

As described in Sec. 4.5.1, to switch off a hologram of a lens, an electric field of about $\pm 2kV/cm$ is required. In this section, the results on multiplexing holograms of lenses and their switching are presented. Fig. 4.17 (a) shows the multiplexing of holograms of two lenses with focal lengths 40 cm and 60 cm, respectively. The multiplexing is done according to Rayleigh's criterion (see Sec. 4.4) and results match quite well with this criterion. Fig. 4.17 (b) shows the multiplexing of holograms of lenses with a hologram of a plane wave.

For the multiplexing of two holograms of lenses (as shown in Fig. 4.17 (a)), one hologram of

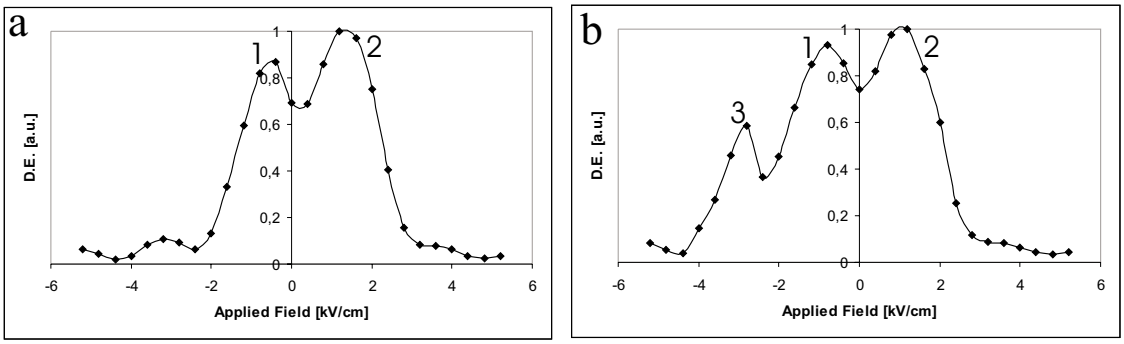

Figure 4.17: Diffraction efficiency as a function of applied field for (a) multiplexing of holograms of lenses with focal length (1) 40cm recorded at $E_{ext} = 0$ and (2) 60 cm recorded at $E_{ext} = +2kV/cm$, (b) multiplexing of the hologram of lenses (1) and (2) with hologram of plane wave recorded at recorded at $E_{ext} = -2kV/cm$(3).

a lens is recorded without application of the field to the crystal and then the next hologram of the second lens was recorded at +2kV/cm and then diffraction efficiency was measured by varying the applied field. The shift in the peak diffraction efficiency of the holograms is again attributed to the photovoltaic field as explained in the previous section. Similarly for the case of multiplexing of three holograms (as shown in Fig. 4.17 (b)), in addition to the two holograms of lenses, already multiplexed, the hologram of a plane wave was recorded at -2kV/cm. Just with a change of the electric field by $\pm 2kV/cm$, three holograms could be switched on and off. With the switching of lenses, we could demonstrate that the crystal containing the holograms acts as a lens with electrically switchable focal length.

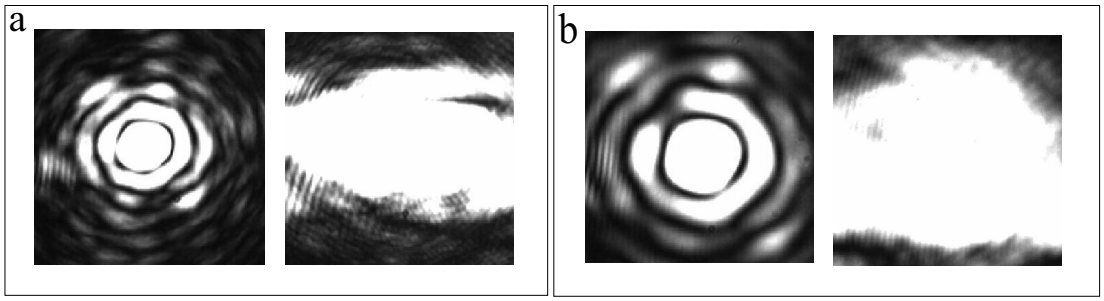

Figure 4.18: Actual and reconstructed focal distribution for the lens with focal length (a) 40cm, (b) 60 cm.

Fig. 4.18 (a) and (b) show the actual focal distribution and the reconstructed focal distribution of the two lenses at their focal planes. Ideally, an infinitely extended plane wave incident on a lens must be focused almost to a point at the focal plane of the corrected lens. The actual focal distribution resembles an Airy pattern which is supposed to approach a delta function distribution in the limit of the aperture radius going to infinity. However,

the reconstructed focal distributions are distorted and not very clear. This problem is attributed to the quality of the crystals.

The crystals were regularly used in experiments with constant recording of holograms and thereafter erasure using homogeneous illumination. The crystals were cleaned by keeping it under uniform illumination for about 12 hours and then again tested by taking some pictures of the transmitted beam. However, this did not improve the situation and the distortions were present after the introduction of the cleaned crystal in the beam. Then, we sought to thermal cleaning of the crystal. The crystal was kept in oven for about 24 hours with specific heating program fed to the programmable oven. It was meant to heat the crystal in steps of $20°/hour$ and then leave at maximum temperature of 165° and then again adiabatic cooling with drop of temperature at the rate $10°/hour$. Such a program ensured safe cleaning of the crystal without destroying it.

This properly cleaned crystal when tested for distortions showed negligible distortions only. However, after recording only one hologram in the cleaned crystal, there were again distortions in the focal distribution. The possible explanation is that the earlier recorded hologram do not get erased and stay in the crystal and these remains of earlier holograms scatter the input beam to the crystal and introduce distortions to it. For this reason, we had to go for frequent thermal cleaning of the crystals. The conclusion is that crystal quality is major cause of worry to avoid distortions to the beam and the focal distribution.

4.6 Electrical Switching of Holographic Mirrors

In this section, electrically switchable holographic mirrors will be demonstrated. Further details on these results can be found in [48]. Fig. 4.19 shows the experimental set-up for the recording of holograms of mirrors. The term holograms of mirrors is used for holograms of plane waves coming from different directions and the mirrors are used to deflect the two recording plane waves. Initially I tried to change the direction of the recording beam just by tilting the mirror and also by inserting a thick glass plate for refracting the beam in a different direction. Both these processes gave very little deflection to the beam and the shift was not clearly observable. Then, we sought out for the interferometer geometry to have a large angle between the two recording beams. As shown in the experimental set-up, the two signal beams σ_1 and σ_2 enter the crystal on either side of the reference beam ρ. Both the signal beams overlap with the reference beam at the same point in the crystal. The process of recording the hologram remains the same as explained in Sec. 4.4. One of the signal beam is blocked and the hologram of one mirror is recorded without application of the field to the crystal. Then the field of 2kV/cm (EFS) is applied to the crystal and the hologram of the second mirror is recorded by blocking the first recording beam now. So, the holograms of mirrors were multiplexed in lithium niobate crystal and then switched using the externally applied field.

Fig. 4.20 shows the read-out of the holograms of two mirrors. Two tilted gratings (holo-

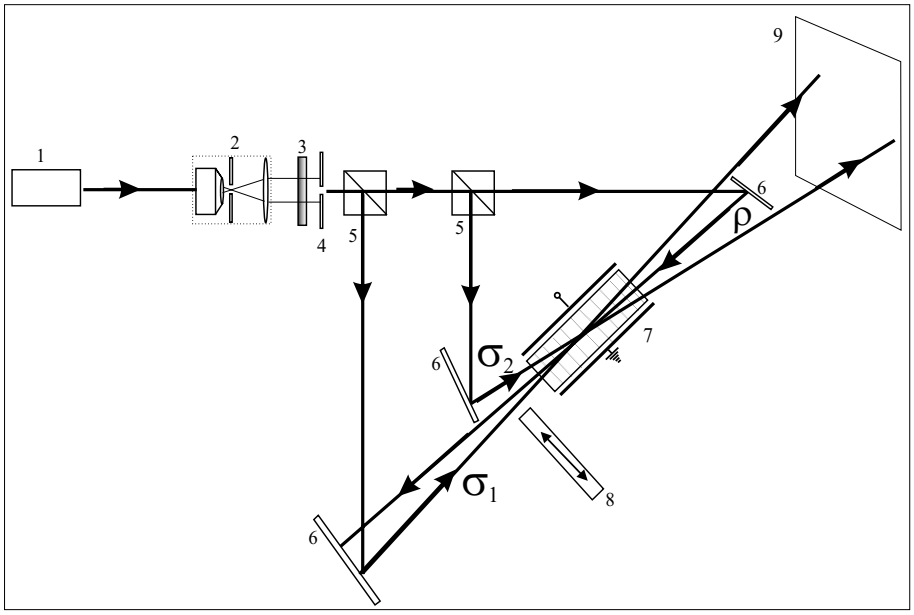

Figure 4.19: The experimental set-up for the recording and read-out of the holograms of mirrors, 1- Nd:YAG cw laser, λ=532 nm , 2 - beam expander, 3 - polarizer, 4 - diaphragm, 5 - beam splitter, 6 - mirror, 7 - crystal with electrodes, 8 - shutter, 9 - screen.

grams) are multiplexed corresponding to the two mirrors at different values of the applied field as explained earlier. While reading out, at a particular value of the applied field, the corresponding hologram is reconstructed. So, just by applying field of 2kV/cm to the crystal, the beam is reconstructed in a different direction (holograms of mirror implies a hologram of the plane wave coming from different directions). This way, the switching of direction of the reconstructed beam could be demonstrated. The angle (θ) between the

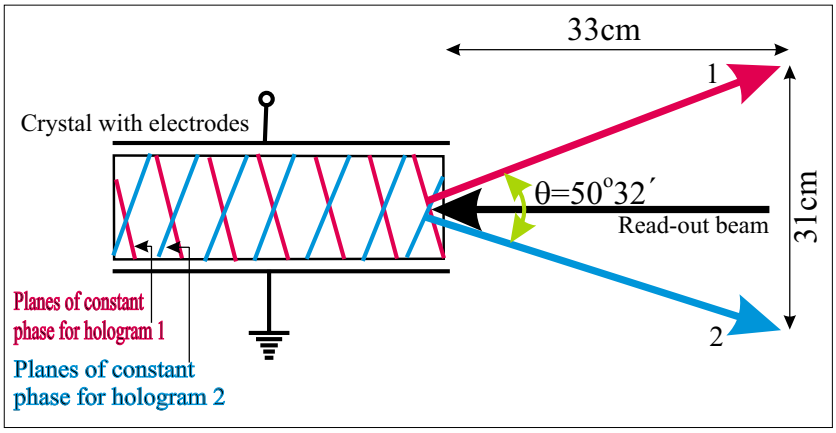

Figure 4.20: Read-out of hologram of mirror 1 and mirror 2.

Figure 4.21: Picture showing the experimental set-up and the location of the reconstructed beams with a field of 1 kV/cm applied to the crystal (both the holograms are reconstructed).

two reconstructed beams can be calculated using simple relations of trigonometry and it comes out to be 50°32′ as shown in Fig. 4.20. However, this angle could be further increased and is limited by the dimensions of the crystal and the diameter of the beams only. For pointed beams and for the crystal used, the maximum angle achievable was 77°32′. Fig. 4.21 shows the picture of the experimental set-up and shows the location of the two reconstructed beams as well.

Fig 4.22 shows the pictures demonstrating the switching of direction. These pictures were taken with a digital camera at three different values of field applied to the crystal. When no field is applied to the crystal, only hologram '1' will be reconstructed and when field with value equal to EFS (where the second hologram is recorded) is applied, only hologram '2' will be reconstructed and when an intermediate value of field is applied, both the holograms are reconstructed simultaneously and one can see both the beams on the screen (as shown in Fig 4.22 (2)). The behavior of the diffraction efficiency with applied field was measured for the two holograms of the mirrors recorded in the crystal with d=2.5 mm, by placing the photodetector at the position of one reconstructed beam and then at the position of the other reconstructed beam. Both the curves are plotted in one diagram and are shown in Fig. 4.23. At very precise recording conditions, cross-talk of less than 10% was observed.

Such a system can be competitive with similar existing application of optical switching for

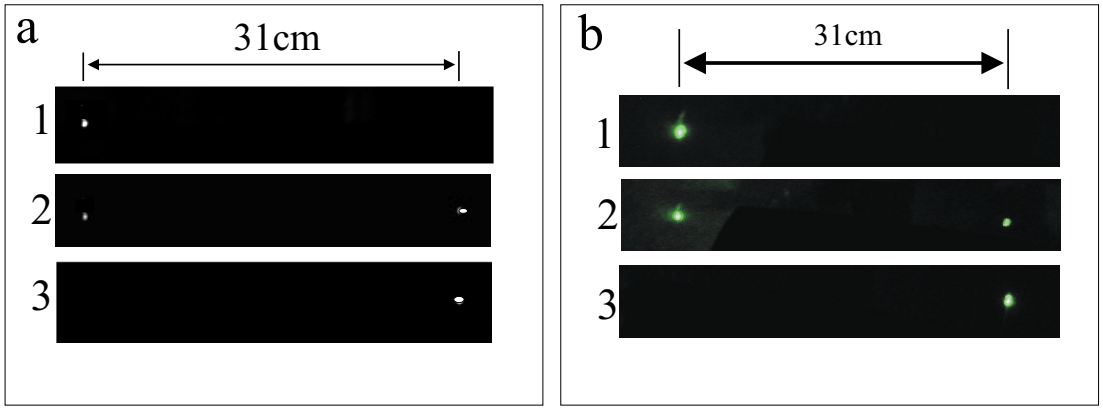

Figure 4.22: Pictures showing switching of holograms of mirrors on a screen for crystal with thickness, (a) d=1 mm and (b) d=2.5 mm; at three values of applied field , 1: E=0, 2: E=1kV/cm and 3: E=2kV/cm.

switching of direction like acousto-optic scanners and deflectors and MEM devices [49,50]. MEM devices can give large angular deflection in the range of 50-60 degrees, but due to high inertia switching speed is limited to few hundred milliseconds. Acousto-optic deflectors have comparatively high switching speed, but these are complex systems and quite expensive, too. The system of switching of holograms of mirrors as demonstrated by me gives angular deflection in the range 0-60 degrees and switching time of few hundred microseconds (as will be discussed in the next section).

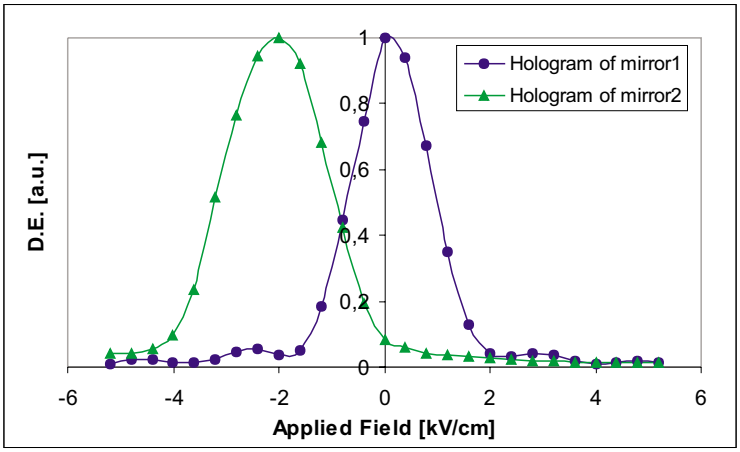

Figure 4.23: Diffraction efficiency as a function of the applied field for the holograms of mirrors.

4.7 Switching Time Analysis

The electro-optic effect is considered to act very fast. Ideally, the time difference in the application of the field and the change of refractive index of the material should be a few nanoseconds, which is the time taken by an electron to change its orbit (electro-optic effect at the sub-atomic level). As this effect was used for switching of the holograms of the lenses and mirrors, it was important to have an estimation of the actual switching time. Other existing optical switching devices for tuning or switching the focus of a beam, like MEM (micro-electro-mechanical) devices and liquid crystal lenses have switching times in the range of few milliseconds.

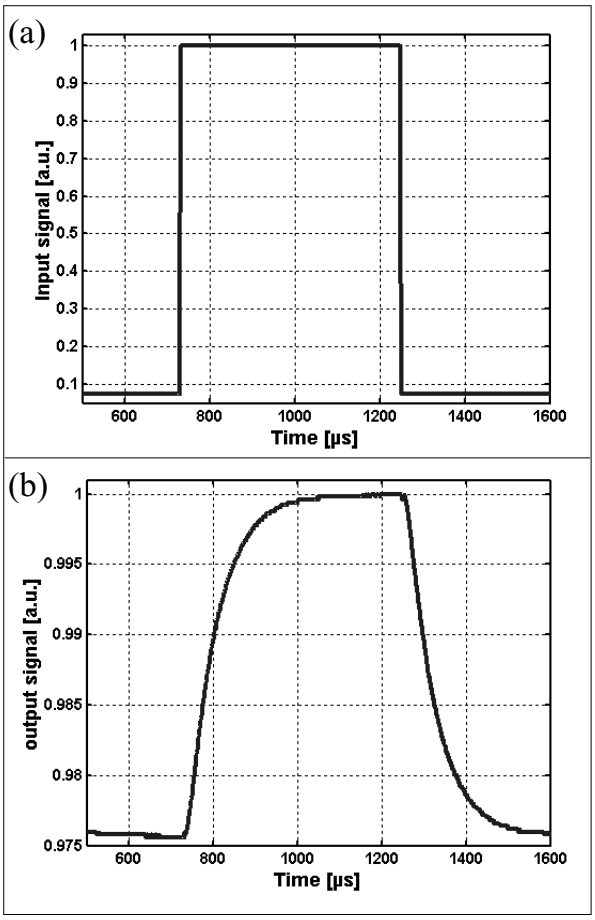

Figure 4.24: (a) Applied input voltage signal and (b) measured temporal behavior of diffraction efficiency for the crystal with thickness d=2.5 mm.

For the estimations of the switching time, a square pulsed voltage supply at 1 kHz frequency was used instead of the continuously tunable dc voltage supply. A digital oscilloscope was used for capturing the data. Corresponding to the input pulsed voltage applied to the

crystal, the output signal obtained from a photo-multiplier detecting the reconstructed beam was captured. The data was measured using a software for grabbing the data and waveforms from the digital oscilloscope using an interface with PC. The data was recorded in 2500 steps for about 2 ms. The measured data for the input square voltage pulse as a function of time and the output signal showing the behavior of diffraction efficiency with time for the crystal with thickness d = 2.5 mm, is shown in Fig. 4.24. Fig. 4.25 shows the picture of the four lithium niobate crystals used for experiments, which have the same doping but differ only in thickness.

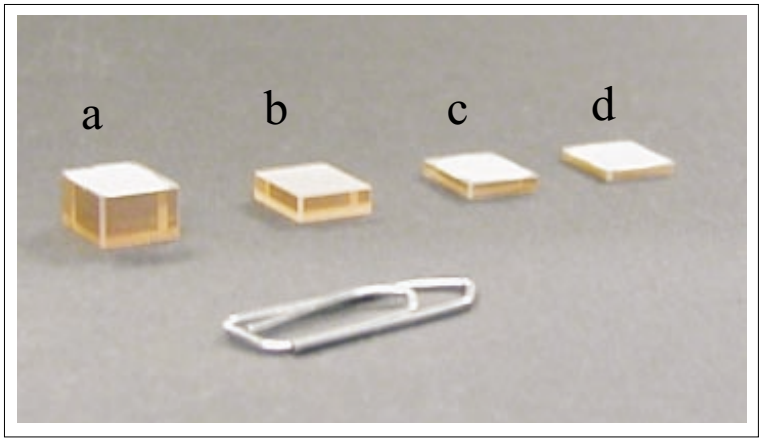

Figure 4.25: Lithium niobate crystals used for experiments, with same doping, but different thickness, d: (a) 5 mm, (b) 2.5 mm, (c) 1.5 mm, (d) 1.0 mm (comparison of dimensions with a paper clip).

The plot for behavior of the diffraction efficiency (output signal) with time as shown in Fig. 4.24 resemble with the charging and discharging curve for a capacitor as shown in Fig. 4.26. So, we could compare the crystal with electrodes and with a voltage V applied to it to an equivalent RC circuit as shown in Fig. 4.27. All RC circuits have a time constant associated with them which is $R{*}C$ and so such circuits take time before the voltage reaches to an equilibrium level. So, we could expect the switching time for switching the holograms to be limited by an RC-time constant of the RC circuit so-formed by the dielectric crystal between the electrodes.

The crystal of lithium niobate with dielectric permittivity, ε, and of thickness, d between the electrode plates of area, $A = w \times T$, can be considered as a capacitor with capacitance, C given by

$$C = \frac{\varepsilon\varepsilon_0 A}{d} \tag{4.37}$$

where ε_0 is the dielectric permittivity of free space.

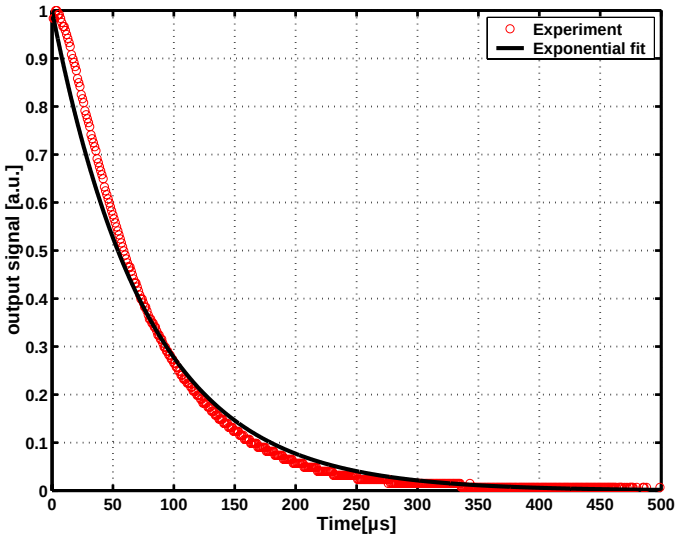

Figure 4.26: measured temporal behavior of diffraction efficiency fitted to the exponential decay curve for a capacitor with RC-time constatnt = 100 μs.

So, the capacitance of the four crystals with different thickness d was calculated and it came out to be $C_1 = 52.04pF$ for d=1 mm, $C_2 = 34.92pF$ for d=1.5 mm, $C_3 = 20.82pF$ for d=2.5 mm and $C_4 = 10,48pF$ for d=5 mm. The resistance of these four crystals between the electrodes was also measured and the RC-time constant was calculated and it came out to be about 100 μs for all four crystals. Also, from Fig. 4.26, the RC-time constant was calculated by fitting the theoretical plots ($e^{-t/RC}$) to the exponential decay curve of capacitor in an RC circuit (Fig. 4.27), with similar RC time constant. The RC-time constant is the time, where the voltage is dropped to $1/e$ of its final steady state value. By fitting the experimental curve to the simulated exponential decay curve (Fig. 4.26) of an

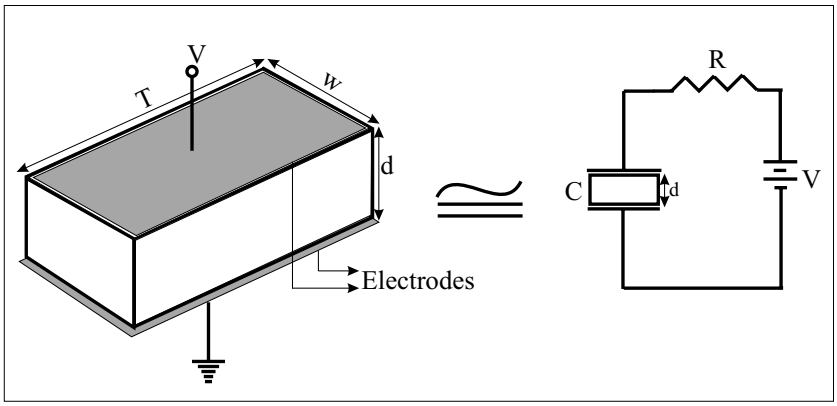

Figure 4.27: Simplified equivalent RC circuit of the crystal with electrodes with a voltage applied to it.

equivalent capacitor, the time constant estimated to be about 100 μs for all four crystals. As this is the limiting factor for switching speed, we concluded this as the switching time for switching the holograms.

4.8 Limitations

It is also important to add limitations and considerations regarding experimental techniques, to help in the future study in this area. Using reflection geometry for recording, which is very sensitive even to small vibrations, special care must be taken while recording the hologram. With a small vibration, the entire hologram may shift and depletion of the signal can be seen while recording. The doping of the crystals must be an important consideration. If the crystals are not sensitive enough, one has to use longer recording times to get appreciable diffraction efficiency, which makes the recording more prone to surrounding conditions imparting vibrations.

To reduce the voltage requirements, if the crystal thickness (separation between the electrodes) is reduced, this may lead to larger capacitance of the system if the area of the electrodes is not reduced and hence switching time will be further limited. So, the thickness of the crystal and the size of electrodes has to be carefully chosen. Implementing the electrical control of diffraction to integrated optics will definitely reduce the switching time. Further, in case of recording holograms of lenses, one can record beams with large beam diameters provided the crystal has equivalently large square cross-section facing the beam. This will require increasing the thickness and the width of the crystal. First factor will lead to larger voltage requirements and later one leads to larger capacitance of the system (by increasing the area of electrode plates). This puts a limitation on the beam diameter that can be used.